

**Synthesis and Characterization of Cu-MOF/MoS<sub>2</sub>  
Nanocomposite for Methylene Blue Dye Removal Studies.**



By

Kiran Basharat

(Registration No: 00000361735)

Department of Materials Engineering  
School of Chemical and Materials Engineering  
National University of Sciences & Technology (NUST)

Islamabad, Pakistan

(2024)

**Synthesis and Characterization of Cu-MOF/MoS<sub>2</sub>  
Nanocomposite for Methylene Blue Dye Removal Studies.**



By

Kiran Basharat

(Registration No: 00000361735)

A thesis submitted to the National University of Sciences and Technology, Islamabad,

in partial fulfillment of the requirements for the degree of

Master of Science in  
Materials and Surface Engineering

Supervisor: Dr. Usman Liaqat

School of Chemical and Materials Engineering

National University of Sciences & Technology (NUST)

Islamabad, Pakistan

(2024)

# THESIS ACCEPTANCE CERTIFICATE



## THESIS ACCEPTANCE CERTIFICATE

Certified that final copy of MS Thesis entitled "Synthesis & Characterization of Cu-MOF/MoS<sub>2</sub> Nanocomposite for Methylene Blue Dye Removal Studies" written by Ms Kiran Basharat (Registration No 00000361735), of School of Chemical & Materials Engineering (SCME) has been vetted by undersigned, found complete in all respects as per NUST Statues/Regulations, is free of plagiarism, errors, and mistakes and is accepted as partial fulfillment for award of MS degree. It is further certified that necessary amendments as pointed out by GEC members of the scholar have also been incorporated in the said Thesis.

Signature: \_\_\_\_\_

Name of Supervisor: Dr Usman Liaqat

Date: 20-11-24

Signature (HOD): \_\_\_\_\_

Date: 20-11-24

Signature (Dean/Principal): \_\_\_\_\_

Date: 21/11/24

TH - 4



National University of Sciences & Technology (NUST)

FORM TH-4

MASTER'S THESIS WORK

We hereby recommend that the dissertation prepared under our supervision by  
Regn No & Name: 00000361735 Kiran Basharat

Title: Synthesis & Characterization of Cu-MOF/MoS<sub>2</sub> Nanocomposite for Methylene Blue Dye Removal Studies.

Presented on: 14 Nov 2024 at: 1530 hrs in SCME

Be accepted in partial fulfillment of the requirements for the award of Masters of Science degree in Materials & Surface Engineering.

Guidance & Examination Committee Members

Name: Dr Zakir Hussain

Signature: [Signature]

Name: Dr Muhammad Arfan

Signature: [Signature]

Name: Dr Waheed Miran (Co-Supervisor)

Signature: [Signature]

Supervisor's Name: Dr Usman Liaqat

Signature: [Signature]

Dated: 15-11-24

[Signature]  
Head of Department

18-11-24  
Date

COUNTERSIGNED

Date \_\_\_\_\_

[Signature]  
Dean/Principal

## **AUTHOR'S DECLARATION**

I Kiran Basharat hereby state that my MS thesis titled “Synthesis and Characterization of Cu-MOF/MoS<sub>2</sub> Nanocomposite for Methylene Blue Dye Removal and its Adsorption Studies.” is my own work and has not been submitted previously by me for taking any degree from National University of Sciences and Technology, Islamabad or anywhere else in the country/ world.

At any time if my statement is found to be incorrect even after I graduate, the university has the right to withdraw my MS degree.

Name of Student: Kiran Basharat


Date: October 2024

## **PLAGIARISM UNDERTAKING**

I solemnly declare that research work presented in the thesis titled “Synthesis and Characterization of Cu-MOF/MoS<sub>2</sub> Nanocomposite for Methylene Blue Dye Removal and its Adsorption Studies.” is solely my research work with no significant contribution from any other person. Small contribution/ help wherever taken has been duly acknowledged and that complete thesis has been written by me.

I understand the zero-tolerance policy of the HEC and National University of Sciences and Technology (NUST), Islamabad towards plagiarism. Therefore, I as an author of the above titled thesis declare that no portion of my thesis has been plagiarized and any material used as reference is properly referred/cited.

I undertake that if I am found guilty of any formal plagiarism in the above titled thesis even after award of MS degree, the University reserves the rights to withdraw/revoke my MS degree and that HEC and NUST, Islamabad has the right to publish my name on the HEC/University website on which names of students are placed who submitted plagiarized thesis.

Student Signature:  \_\_\_\_\_

Name: Kiran Basharat

## **DEDICATION**

*“By the grace of Almighty Allah, who is the most Beneficent and the most merciful  
This research is dedicated to my parents, for their unconditional love, support,  
sacrifices, prayers, and advice. To my supervisor who shared his knowledge, gave  
advice, and encouraged me to fulfill my tasks. And to all my fellows, with whom I  
worked with and shared good memories.”*

## ACKNOWLEDGEMENTS

I am most grateful to **Allah** for His mercy and generosity in guiding me during my academic career. This work would not have been possible without the supernatural inspiration and assistance I have been graced with.

My parents, **Salma Naz**, and **Basharat Mahmood**, have sincere gratitude for their constant support and faith in my abilities, which have been the cornerstones of my success. I am incredibly grateful to my **FAMILY** for their unwavering love and support, which has given me incredible strength.

I also want to thank **Dr. Usman Liaqat**, whose guidance and assistance have been crucial to this research. Under Dr. Hussain's supervision, my work has taken a new direction, and I have had many opportunities to gain experience personally and academically.

I appreciate the thoughtful comments and helpful critiques provided by my co-supervisor **Dr. Waheed Miran** and GEC Members **Professor Dr. Muhammad Arfan** and **Professor Dr. Zakir Hussain**, the other committee members. Their knowledge and varied viewpoints have greatly improved the study's approach and substance.

In addition, I would like to thank my sister **Mariam Basharat**, and friends **Hafsa Yousaf**, and **Muhammad Waqas Khalil** for their support and help; their friendship and teamwork have made my research experience much more enjoyable. I would especially like to thank my lab fellow **Umar Farooq Shah** and lab engineers, for their invaluable technical support. I appreciate **Abdul Ahad Khan's** assistance and the lab members who supported me throughout difficult moments.

These people have all profoundly affected my life, personally and professionally, and I will always appreciate what they have done to help me along the way.

Kiran Basharat



## TABLE OF CONTENTS

<b>ACKNOWLEDGEMENTS .....</b>	<b>viii</b>
<b>LIST OF TABLES.....</b>	<b>xii</b>
<b>LIST OF FIGURES .....</b>	<b>xiii</b>
<b>LIST OF SYMBOLS, ABBREVIATIONS and acronyms .....</b>	<b>xiv</b>
<b>ABSTRACT.....</b>	<b>xv</b>
<b>CHAPTER 1: INTRODUCTION.....</b>	<b>1</b>
1.1    Background.....	1
1.2    Objective.....	2
<b>CHAPTER 2: LITERATURE REVIEW.....</b>	<b>3</b>
2.1    Dye.....	3
2.1.1    Types of Dyes .....	3
2.1.2    Factors Affecting Dye Adsorption .....	3
2.2    Methylene Blue dye .....	4
2.2.1    Properties .....	4
2.2.2    Sources of MB dye.....	5
2.2.3    Applications of Methylene Blue dye .....	5
2.2.4    Harmful effects of Methylene Blue dye.....	5
2.3    Metal-Organic Frameworks .....	6
2.3.1    Introduction.....	6
2.3.2    Synthesis of MOF .....	7
2.4    Cu-MOF .....	8
2.4.1    Characteristics of Cu-MOF .....	9
2.4.2    Applications of Cu-MOF .....	9
2.5    2D Materials.....	10
2.5.1    Introduction.....	10
2.5.2    What are Two-Dimensional (2D) Materials?.....	11
2.5.3    Why Two-Dimensional (2D) Materials? .....	12
2.5.4    Examples of 2D materials.....	13
2.5.5    Bottom-up Synthesis of 2D Materials.....	16
2.5.6    Top-Down synthesis of 2D Materials .....	17
2.6    Molybdenum Disulphide .....	18
2.6.1    Properties of MoS <sub>2</sub> .....	19

2.6.2	Application of MoS <sub>2</sub> .....	20
2.7	Role of Nanotechnology in Wastewater Treatment .....	21
2.8	Adsorption Study .....	22
2.8.1	Background .....	22
2.8.2	Adsorption Isotherms .....	23
2.8.3	Adsorption Kinetics .....	25
<b>CHAPTER 3:</b>	<b>MATERIALS AND METHODS.....</b>	<b>27</b>
3.1	Materials and Chemicals Utilized .....	27
3.2	Methodology .....	27
3.2.1	Synthesis of Cu MOF (HKUST-1, Cu-BTC OR MOF-119) .....	27
3.2.2	Exfoliation of Bulk MoS <sub>2</sub> by Probe Sonication Method.....	28
3.2.3	In-Situ Synthesis of Exfoliated MoS <sub>2</sub> /Cu-MOF Nanocomposite .....	29
<b>CHAPTER 4:</b>	<b>CHARACTERIZATION.....</b>	<b>32</b>
4.1	Instruments.....	32
4.2	SEM .....	32
4.2.1	Sample Preparation .....	33
4.3	XRD .....	33
4.3.1	Sample Preparation .....	35
4.4	FTIR.....	35
4.4.1	Sample Preparation .....	36
4.5	Raman Spectroscopy.....	36
4.5.1	Sample Preparation .....	37
4.6	AFM.....	38
4.6.1	Sample Preparation .....	39
4.7	UV-Vis Spectroscopy .....	39
4.7.1	Sample Preparation .....	40
<b>CHAPTER 5:</b>	<b>RESULTS AND DISCUSSION.....</b>	<b>41</b>
5.1	Scanning Electron Microscopy .....	41
5.2	X-ray diffraction Analysis.....	42
5.3	Fourier Transform Infra-Red Spectroscopy .....	44
5.4	AFM.....	46
5.5	Adsorption Study .....	47
5.5.1	Stock Solution.....	47

5.5.2	Experimentation .....	47
5.5.3	Effect of Contact time on Adsorption .....	48
5.5.4	Effect of adsorbent dosage on adsorption of MB .....	49
5.5.5	Effect of initial concentration of MB on adsorption .....	50
5.6	Adsorption Kinetics .....	51
5.6.1	Pseudo-first order Model .....	51
5.6.2	Pseudo-second order Model.....	52
5.7	Adsorption Isotherm .....	54
5.7.1	Langmuir Isotherm Model .....	54
5.7.2	Freundlich Isotherm Model.....	55
<b>CHAPTER 6: CONCLUSIONS .....</b>		<b>58</b>
FUTURE RECOMMENDATIONS:.....		58
<b>REFERENCES.....</b>		<b>59</b>

## LIST OF TABLES

<b>Table 2.1:</b> List of Adsorbents (MoS <sub>2</sub> and Cu-MOF) for Adsorption of Organic Dye Reports in Recent Years.....	21
<b>Table 3.1:</b> Experimental conditions for several synthesized samples .....	30
<b>Table 5.1:</b> % Absorbance of Cu-MOF, MoS <sub>2</sub> and Cu-MOF/MoS <sub>2</sub> Nanocomposite with respect to Time .....	48
<b>Table 5.2:</b> % Absorbance of Cu-MOF, MoS <sub>2</sub> and Cu-MOF/MoS <sub>2</sub> Nanocomposite with respect to adsorbent dosage.....	49
<b>Table 5.3:</b> % Absorbance of Cu-MOF, MoS <sub>2</sub> and Cu-MOF/MoS <sub>2</sub> Nanocomposite with respect to Initial concentration of MB. ....	50
<b>Table 5.4:</b> Non-linear analysis of kinetic adsorption parameters for MB dye removal by Cu-MOF, MoS <sub>2</sub> and Cu-MOF/MoS <sub>2</sub> .....	54
<b>Table 5.5:</b> Freundlich Isotherm Model for Cu-MOF, MoS <sub>2</sub> and Cu-MOF/MoS <sub>2</sub> Nanocomposite.....	56

## LIST OF FIGURES

<b>Figure 2.1:</b> The molecular arrangement of MB .....	4
<b>Figure 2.2:</b> MOF structure formed through the establishment of chemical bonds between metal ions as nodes and organic molecules as linkers .....	7
<b>Figure 2.3:</b> Standard solvothermal synthesis process. ....	8
<b>Figure 2.4:</b> Schematic representation of Cu-MOF structure. ....	9
<b>Figure 2.3:</b> Chronological compilation of publications on 2D materials [25]. ....	11
<b>Figure 2.4:</b> The 2D materials genus. (a) The most generally recognized two-dimensional layered materials are the highlighted components of the periodic table. (b,c) The Family classification of the 2D material and the Family of Transition Metal Dichalcogenides (TMDCs). (d) The generic formula of MX <sub>2</sub> in transition metal dichalcogenides (TMDCs) is consistent with the layered structure of MoS <sub>2</sub> . ....	14
<b>Figure 2.5:</b> Examples of 2D Materials. ....	16
<b>Figure 2.6:</b> Bottom-Up Synthesis Methods of 2D Materials. ....	17
<b>Figure 2.7:</b> Top-Down Synthesis Methods of 2D Materials. ....	18
<b>Figure 2.8:</b> MoS <sub>2</sub> structure showing Mo sandwiches between two sulfur atom layers. ....	19
<b>Figure 3.1:</b> Schematics of Cu-MOF synthesis .....	28
<b>Figure 3.2:</b> Schematics of Chemical Exfoliation of Bulk MoS <sub>2</sub> by Adding Liquid Nitrogen. ....	28
<b>Figure 3.2:</b> Schematics of Bulk MoS <sub>2</sub> by Probe Sonication Method .....	29
<b>Figure 3.3:</b> Schematics of Exfoliated MoS <sub>2</sub> @Cu-MOF Nanocomposite synthesis. ....	30
<b>Figure 4.1:</b> Interaction between an electron beam and a specimen .....	33
<b>Figure 4.2:</b> Mechanism of action of X-ray diffraction (XRD). ....	34
<b>Figure 4.3:</b> Illustration of the functioning of FTIR spectroscopy .....	36
<b>Figure 4.4:</b> Assembly of the Raman spectroscopy. ....	37
<b>Figure 4.5:</b> The AFM principle .....	38
<b>Figure 4.6:</b> A demonstration of the principle of UV spectroscopy .....	40
<b>Figure 5.1:</b> SEM Results of investigated Cu-MOF (A,B), Bulk MoS <sub>2</sub> (C), MoS <sub>2</sub> (D,E) and Cu-MOF/MoS <sub>2</sub> Nanocomposite (F,G). ....	42
<b>Figure 5.2:</b> XRD Results of investigated Cu-MOF, MoS <sub>2</sub> and Cu-MOF/MoS <sub>2</sub> Nanocomposite. ....	44
<b>Figure 5.3:</b> FTIR Results of investigated Cu-MOF, MoS <sub>2</sub> and Cu-MOF/MoS <sub>2</sub> Nanocomposite. ....	46
<b>Figure 5.4:</b> AFM of Bulk MoS <sub>2</sub> and MoS <sub>2</sub> Nanosheets. ....	47
<b>Figure 5.4:</b> Trend of removal efficiency of Cu-MOF, MoS <sub>2</sub> and Cu-MOF/MoS <sub>2</sub> Nanocomposite with respect to Time. ....	49
<b>Figure 5.5:</b> Trend of removal efficiency of Cu-MOF, MoS <sub>2</sub> and Cu-MOF/MoS <sub>2</sub> Nanocomposite with respect to adsorbent dosage. ....	50
<b>Figure 5.6:</b> Pseudo first order for Cu-MOF, MoS <sub>2</sub> and Cu-MOF/MoS <sub>2</sub> Nanocomposite. ....	52
<b>Figure 5.7:</b> Pseudo second order for Cu-MOF, MoS <sub>2</sub> and Cu-MOF/MoS <sub>2</sub> Nanocomposite. ....	53
<b>Figure 5.8:</b> Langmuir Isotherm Model for Cu-MOF, MoS <sub>2</sub> and Cu-MOF/MoS <sub>2</sub> Nanocomposite. ....	55
<b>Figure 5.9:</b> Freundlich Isotherm Model for Cu-MOF, MoS <sub>2</sub> and Cu-MOF/MoS <sub>2</sub> Nanocomposite .....	56

## LIST OF SYMBOLS, ABBREVIATIONS AND ACRONYMS

MOFs	Metal-Organic Framework
NPs	Nanoparticles
Cu	Copper
MB	Methylene Blue
Mo	Molybdenum
S	Sulfur
MoS <sub>2</sub>	Molybdenum Disulfide
2D	2 Dimensional
SEM	Scanning Electron Microscopy
XRD	X-Ray Diffraction
FTIR	Fourier Transform Infra-Red Spectroscopy
AFM	Atomic Force Microscopy
UV-Vis	Ultraviolet Visible
TMDC	Transition Metal Dichalcogenides
(Cu (NO <sub>3</sub> ) <sub>2</sub> )	Copper II Nitrate
BTC	benzene tricarboxylic acid
NMP	N-Methyl pyrrolidone
IR	Infrared
KBr	Potassium bromide
PFO	Pseudo first order
PSO	Pseudo second order
MO	Methyl Orange
DI water	Deionized water

## ABSTRACT

This study investigates the adsorption ability of 2D MoS<sub>2</sub> combined with Cu-MOF for methylene blue (MB) by synthesizing several nanocomposites by an in-situ process at room temperature, incorporating varied weight percentages of 2D MoS<sub>2</sub>. Consequently, the Cu-MOF/MoS<sub>2</sub> (9%) nanocomposite showed superior performance compared to other nanocomposites for the adsorption of MB from wastewater, achieving an adsorption efficiency of 89.9%. The synthesized samples' crystal structure, elemental mapping, functional group identification, and morphology were analyzed using SEM, XRD, FTIR, and AFM, respectively.

This study demonstrates a recent type of adsorbent material: the nanocomposite of molybdenum disulfide (MoS<sub>2</sub>) with the copper metal-organic framework (Cu-MOF). The characteristics of 2D (two-dimensional) MoS<sub>2</sub> structures, including a high absorption coefficient, elevated surface-to-volume ratio, and adjustable band gap, render them a promising candidate in diverse domains such as electronics, energy storage, catalysis, and adsorption. Metal-organic frameworks (MOFs) have emerged as a sophisticated category of materials, and they have been recognized for their efficacy as adsorbents during the past two decades due to their straightforward production, extensive surface area, and customizable pore dimensions. Metal-organic frameworks (MOFs) are recognized as effective agents for removing dyes from wastewater.

This study investigates the adsorption ability of 2D MoS<sub>2</sub> combined with Cu-MOF for methylene blue (MB) by synthesizing several nanocomposites by an in-situ process at room temperature, incorporating varied weight percentages of 2D MoS<sub>2</sub>. Consequently, the Cu-MOF/MoS<sub>2</sub> (9%) nanocomposite showed superior performance compared to other nanocomposites for the adsorption of MB from wastewater, achieving an adsorption efficiency of 89.9%. The crystal structure, elemental mapping, functional group identification, and morphology of the synthesized samples were analyzed using SEM, XRD, FTIR, and AFM, respectively.

Additionally, the impact of time, adsorbent, and adsorbate variations on the adsorption process was investigated. The experimental results were analyzed using kinetic models, specifically the pseudo-first order and pseudo-second-order kinetic models, and according to the results,

pseudo-first order and pseudo-second order with  $R^2 = 0.98$ . Langmuir and Freundlich's adsorption isotherms thoroughly examine the adsorption isotherms of MB on nanocomposites. This research reveals the potential of Cu-MOF/MoS<sub>2</sub> nanocomposite for effectively removing organic dyes from wastewater effluent.



# CHAPTER 1: INTRODUCTION

## 1.1 Background

The access to freshwater is already constrained in numerous regions throughout the globe. [1, 2]. The constraints will intensify further as a result of population growth and climate change. Pollution in freshwater environments will also contribute to this constraint, in addition to the rising demand for water. Pollution diminishes the availability of recycled water and escalates the expense of its purification. Both organic and inorganic substances are major sources of pollution in water. Due to the proximity of most industrial processes near water bodies, these processes are becoming more contaminated with both organic and inorganic pollutants. Potential pollutants interfere with agricultural or industrial water use and harm human health. Effluents from the dyeing industry pose a significant challenge for treatment due to their high chemical oxygen demand and the presence of colour, which is the most noticeable pollutant to the human eye.

Dyes are extensively employed in several industries, such as the production of coloured goods and the manufacturing of rubber, plastics, printing, leather, and textiles, among others. [3] The yearly waste amounts to 280,000 tons of dyes and other chemical compounds, including phosphates and nitrates. [4]. Aside from potentially harming photosynthetic activity, dyes containing aromatics, metals, and other substances may be harmful to certain aquatic species [5]. Because of their harmful consequences, dyes have raised a lot of concerns about their use. It has been linked to chromosomal fractures, mutagenesis, pulmonary toxicity, and carcinogenesis.

In addition to their potential toxicity even at low concentrations, dyes are typically non-biodegradable and pose challenges for removal by standard biological treatment methods like the activated sludge process. [6] Membrane separation, chemical oxidation, aerobic and anaerobic degradation utilizing different microbes, coagulation, and flocculation, adsorption using different types of adsorbents, and reverse osmosis are some techniques for removing dye from wastewater [7].

It is necessary to discover alternative methods that are proficient in eliminating dyes from effluents and are superior in terms of efficiency and cost-effectiveness compared to the existing methods. This is a result of the extant constraints of the treatment methods currently in use, as well as the previously mentioned issues regarding the release of waste materials into the environment.

Adsorption is superior to other methods in terms of its initial cost, adaptability, simplicity of design, convenience of operation, and lack of sensitivity to harmful pollutants. [8]. Additionally, this technique can eliminate or reduce a wide variety of contaminants, which means that it has a larger range of applications in the field of water pollution control. In terms of characteristics, the availability of the adsorbents is the most crucial aspect. Several issues are connected to the adsorption process, including the expense of adsorbent materials, the pre-treatment of those materials, and the process of their regeneration. [9]. The Cu-MOF@MoS<sub>2</sub> is a viable option due to its microporous structure, as well as its substantial adsorption capacity and surface area.

Adsorption is a unit operation that involves the simultaneous attachment of molecules onto a surface. [10]. This hypothesis is employed because of the finding that certain solids have a propensity to selectively absorb other solutes from the solution onto their surfaces. To selectively eliminate dyes, a wide range of diverse adsorbents are employed. Various alternative adsorbents, including activated carbon, zeolites, natural clays, synthetic polymers, metal-organic frameworks, nanomaterials, and others, have been investigated in recent years to assess their potential for chemical removal. Compared to other adsorbents, Cu-MOF@MoS<sub>2</sub> has demonstrated exceptional removal properties. It is a highly porous adsorbent with a substantial surface area, making it suitable for various applications. The targeted application of Cu-MOF@MoS<sub>2</sub> has effectively eliminated methylene blue dye, a commonly utilized dye in the textile sector.

## 1.2 Objective

The main goal of this study is to find out the synthetic strategy for adsorbents that would be environment friendly, easy, reliable, and cheap. The target is to synthesize the adsorbents which would show higher stability, high surface area, stronger host-guest correlation, and appreciative adsorption ability. The key objectives are given below.

1. Exfoliation of bulk MoS<sub>2</sub> into nanosheets and preparation of its nanocomposite with Cu-MOF.
2. Characterization of the prepared samples by using different techniques
3. The applicability of prepared nanocomposite for methyl orange adsorption
4. Investigation of kinetic and adsorption isotherm models
5. Study of the impact of contact time, temperature, and effect of pH on the adsorption process

## CHAPTER 2: LITERATURE REVIEW

### 2.1 Dye

Dyes are materials that, when added to a substrate, give it color through a process that modifies the colored substance's crystal structure, if only momentarily. [11]. These materials, which have a significant ability to color, are used extensively in the paper, plastics, food, textile, pharmaceutical, and photography sectors. The dyes can cling to suitable surfaces through physical adsorption, covalent bond formation, complex formation with metals or salts, or mechanical retention. Dyes have chromophores, which are the parts of molecules responsible for their color, and auxochromes, which enhance the dye's ability to bind to the substrate.

#### 2.1.1 Types of Dyes

Dyes are categorized into numerous types based on their chemical composition, use, and solubility. The following are the primary types of dyes relevant for adsorption studies:

- Anionic Dyes (Acid Red 88, Reactive Black)
- Cationic Dyes (MB)
- Non-Ionic Dyes (Vat Blue 1)
- Zwitterionic Dyes (Reactive Blue 19, Direct Black 38)
- Other Dyes (Allura Red AC, Tartrazine)

#### 2.1.2 Factors Affecting Dye Adsorption

For dye adsorption, several factors must be considered:

- Adsorbent Surface Area and Porosity: Adsorption capacity is normally increased with higher surface area and porosity.
- pH of Solution: pH influences the ionization state of dyes and adsorbents, which influences adsorption efficiency.
- Contact Time: Longer contact times frequently result in increased adsorption until equilibrium is achieved.
- Higher dye concentrations may increase adsorption capacity, but they can also saturate the adsorbent.
- Temperature: This can influence the adsorption process, often increasing adsorption with temperature.

## 2.2 Methylene Blue dye

Methylene Blue (MB) dye is a heterocyclic aromatic chemical with a molecular weight of 319.8 g/mol. The chemical formula is  $C_6H_{18}N_3SCl$ . The compound was first synthesized by Heinrich Caro, a German scientist, in 1876. MB dye is in a solid state at normal room temperature.

The temperature is neutral and there is no discernible scent. The substance manifests as a dark green powder and transforms into a blue solution upon dissolution in water. The hydrated version of MB dye has a water-to-dye ratio of 3:1, with three water molecules per molecule of MB. The MB dye is widely utilized in the disciplines of biology and chemistry. The International Non-proprietary Name (INN) for MB is methylthioninium chloride, which is a pharmaceutical medication now undergoing experimental testing. The World Health Organization has designated it as an indispensable medication that is necessary for a fundamental healthcare system. Methylene Blue (MB) is a positively charged dye that exhibits its highest light absorption at a wavelength of 664 nm.

### 2.2.1 Properties

Molecular formulae	$C_6H_{18}N_3SCl$
Molar mass	319.85 g/mol
Melting point	100-110 °C (with decomposition)
Boiling point	Decomposes

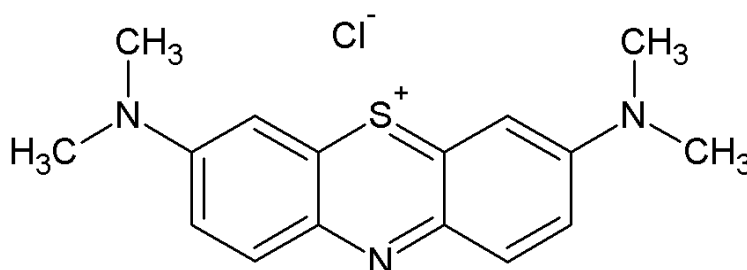


**Figure 2.1:** The molecular arrangement of MB

### 2.2.2 Sources of MB dye

The primary supply originates from the textile industry. Wastewater is produced during the coloring process as a consequence of the bleaching of natural fibers, washing, and the dyeing and finishing phases. Due to the extensive selection of fibers, dyes, and process aides that are employed in a variety of industrial processes. These procedures produce wastewater that contains a wide range of complex and diverse chemicals. However, traditional wastewater treatment plants are not equipped to effectively treat this type of wastewater.

### 2.2.3 Applications of Methylene Blue dye

Methylene blue dye has been commonly utilized to stain nerve fibers, a technique referred to as intravital or supravital staining. This function was initially described in 1887 by Paul Ehrlich. Into the tissue, a weak concentration of the dye is either injected or applied to small, recently extracted sample fragments. The manifestation of the blue colour becomes evident when the stained specimen is exposed to oxygen and can be undone by submerging it in a watery solution of ammonium molybdate. In the past, vital methylene blue was frequently employed to investigate the nerve supply of internal organs, skin, and musculature. The precise mechanism by which dyes selectively enter cells is not fully understood. Nevertheless, the coloration of nerve fibers in the skin can be impeded by ouabain, a drug that inhibits the Na/K-ATPase enzyme present in cell membranes.

The industrial applications are as outlined below:

- Utilized for tinting paper.
- Employed for dyeing leather products.
- Used for dyeing cotton and wool fabrics.
- Employed as a transient hair dye.
- Utilized in the production of paper stock.

### 2.2.4 Harmful effects of Methylene Blue dye

Eliminating colors from contaminated wastewater is a crucial undertaking to safeguard the environment. The effluent from the textile sector has been identified as a significant contributor to wastewater in Asian countries, both in terms of volume and content [12]. Methylene blue is a type of drug called a monoamine oxidase inhibitor (MAOI). If it is given through a vein at doses higher than 5 mg/kg, it can cause a dangerous condition called serotonin toxicity.

Combining it with other medications that increase brain serotonin levels, including selective serotonin reuptake inhibitors (SSRIs) or other serotonin reuptake inhibitors like duloxetine, imipramine, clomipramine, venlafaxine, or sibutramine, can cause this. When the G6PD (favism) enzyme is deficient, it leads to hemolytic anemia.

1. Workers engaged in the process of managing or dealing with Individuals exposed to methylene blue have a significant likelihood of developing photo irritant contact dermatitis (PICD). During inhalation, it might cause intermittent episodes of fast and labored breathing [13].
2. Exposure to large quantities of solid dye can cause damage to the cornea and conjunctiva in humans.
3. Administering high quantities of methylene blue, specifically around 500 mg, has resulted in the manifestation of the subsequent symptoms in individuals. Common symptoms of the condition include nausea, abdominal and precordial pain, dizziness, and headache. Excessive perspiration and cognitive disorientation.
4. Methylene blue is a recognized teratogen that causes intestinal atresia when administered into the amniotic fluid [14].

Methylene blue can potentially cause hemolytic anemia, hyperbilirubinemia, and acute renal failure. Common symptoms include a sensation of burning, vomiting, and diarrhea. [15].

## **2.3 Metal-Organic Frameworks**

### **2.3.1 Introduction**

Porous materials are categorized into three primary classes: microporous zeolites, mesoporous silica, and metal oxides, and macroporous polymer architectures. According to IUPAC, materials are classified based on their pore size. If the pore size is between 0-2 nm, the material is considered mesoporous. If the pore size is less than 50 nm, it is classified as microporous. If the pore size is greater than 50 nm, it is categorized as macroporous. Because of their distinctive attributes and narrow pore size, they are favored options in various industries such as the energy industry, for purposes such as catalysis, adsorption, ion exchange, and host-guest assembly[16]

In general, the porous materials were derived from either organic or inorganic substances. Inorganic porous materials, such as silica or metal oxides, possess a crystalline structure. However, due to their fully inorganic composition, these materials lack structural flexibility, functional tolerability, and mechanical strength. On the other hand, porous materials made of

polymers are either amorphous or partially ordered in poly-crystalline forms, such as diamond or graphite [17]. Organic-inorganic hybrid porous materials, a novel class of substances, have been developed. These materials combine the advantageous features of both organic and inorganic classes, potentially exhibiting extraordinary characteristics that surpass the specific properties of each class [18]

Metal-organic frameworks (MOFs) are a type of inorganic-organic material that is gaining recognition as a new microporous, coordinating polymer. They are considered a class of organic-inorganic hybrid materials and are being studied for their potential in many applications. [19].

MOFs are materials that possess both crystalline and porous characteristics. They consist of metal ions and ligands, which are coupled through a network of organic linkers, as illustrated in **(figure 2.2)**. One notable feature of MOFs is their ability to precisely control their structure, pore size, and usefulness by carefully choosing the metal and organic linker as building pieces and determining their connections. [20].

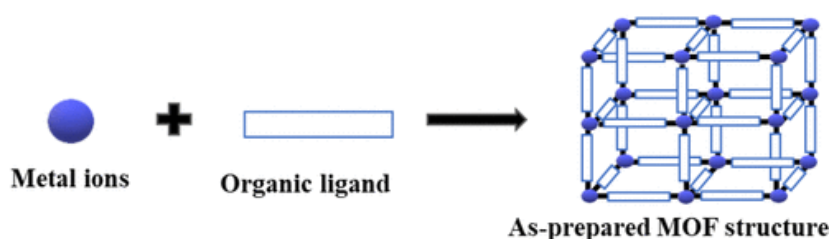


**Figure 2.2:** MOF structure formed through the establishment of chemical bonds between metal ions as nodes and organic molecules as linkers.

### 2.3.2 Synthesis of MOF

The synthesis of a multitude of distinct MOFs has been achieved due to the diverse array of inorganic and organic constituents. The current category of MOF material has over 20,000 distinct structures, as documented in the Cambridge structure database and studied over the past two decades. [21].

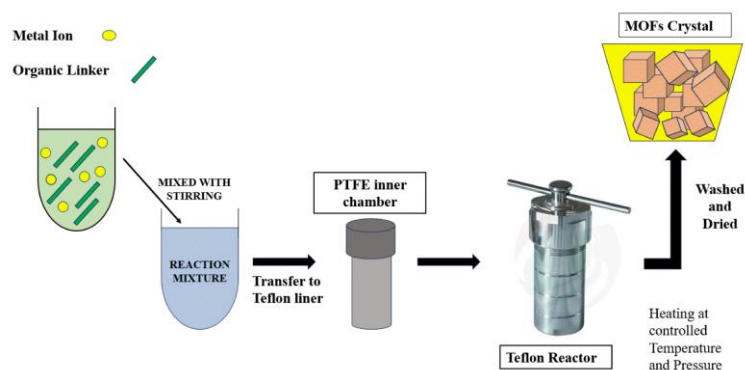


**Figure 2.3:** Standard solvothermal synthesis process.

Usually, solvothermal conditions, which refer to temperatures between 100 °C and 250 °C or room temperature, are employed for the synthesis of MOF crystals (**figure 2.3**). In a typical solvothermal procedure, all the necessary substances (metal salts, ligands, and solvents) are combined in sealed containers. The temperature is then raised slightly below the subcritical point and maintained for minutes, hours, or days, depending on the specific MOF being synthesized.

The primary parameter is temperature because it establishes a condition for the reacting system in a way that maximizes thermodynamically favorable coordination contacts and reactant diffusion, Thus, facilitating the natural formation of organized structures or lattices. Aside from water, the most common solvents include pyridine, alcohols, and dialkyl formamides [22].

## 2.4 Cu-MOF

Since it was one of the first porous MOFs to be found, the Cu-based MOF-199 [Cu<sub>3</sub>(BTC)<sub>2</sub>] has served as a reference for research on several general MOF properties. The three typical microporous sites (5, 11, and 13.5 Å in diameter), that make up the MOF-199 3D framework structure are copper paddle-wheel construction units coupled by organic linkers made of trimesic acid (**fig.2.4**)



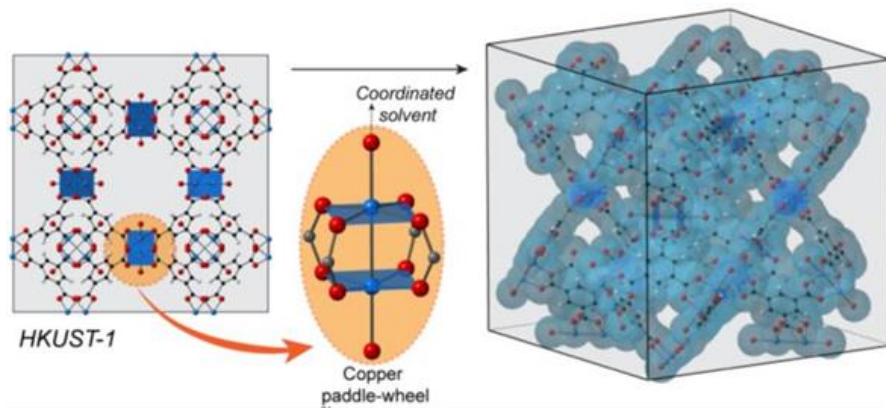


**Figure 2.4:** Schematic representation of Cu-MOF structure.

#### 2.4.1 Characteristics of Cu-MOF

Copper-based materials provide a multitude of beneficial qualities that make them highly attractive for various applications, particularly in the areas of adsorption and catalysis. Some of the characteristics include:

- High Surface Area
- Flexible Pore Size and Volume
- Chemical Stability
- Catalytic Activity
- Selective Absorptivity
- Reusability

#### 2.4.2 Applications of Cu-MOF

Copper-based metal-organic frameworks (Cu-MOFs) have garnered significant attention in recent times due to their adaptable property and potential applications in a variety of industries. These materials, made up of copper ions ( $\text{Cu}^{2+}$ ) bonded with organic ligands, have distinct structural properties that make them well-suited for many technical and industrial uses. Here are some of the applications:

- Gas Storage and Separation
- Catalysis
- Sensing and Detection
- Drug delivery
- Environmental Remediation

- Energy storage and conversion
- Antimicrobial coatings

## 2.5 2D Materials

### 2.5.1 Introduction

The emergence of two-dimensional (2D) materials leads to the ultimate constraint for material thickness; graphene and its counterparts can achieve even a single layer's thickness. Furthermore, the increase in the number of representatives in this class of materials suggests an abundance of diversity in the properties and functionalities of materials, which vary quickly by moving from bulk counterparts to their 2D forms (nanosheets) due to the quantum confinement effect and can also be fine-tuned and merged to form more complicated structures. The literature contains various accounts of layered materials exhibiting strong in-plane bonding and intricate bonding between the layers. The layered designs can separate bulk material into individual atomic layers by exfoliation. The fundamental origin of 2D materials lies in the layered structure of materials, where the intermolecular forces known as Van der Waals forces play a crucial role. Van der Waals materials exhibit stability due to the presence of robust bonding within the layers and relatively weak interlayer forces, known as Van der Waals forces. This structural arrangement makes them suitable for the process of exfoliation.

In recent years, there has been a significant increase in the study of 2D layered materials, which began with the initial separation of graphene from its bulk analogue, graphite [23]. The publication of each new material is met with both enthusiasm and mystery due to the disparities in properties between these 2D materials and their bulk equivalents. In addition, the intriguing 2D library expands annually and possesses an excess of 150 unique materials that can be effortlessly separated into sub-nanometer 2D monolayers. 2D materials encompass transition metal dichalcogenides (TMDCs) like WSe<sub>2</sub>, MoS<sub>2</sub>, WS<sub>2</sub>, hexagonal boron nitride (h-BN), silicene (2D silicone), germanene (2D germanium), borophene (2D boron), and MXenes.[24] **(Figure 2.4)** displays a chronological compilation of publications on 2D materials, categorizing them by year which highlights a growing enthusiasm for investigating transition metal dichalcogenides (TMDCs).

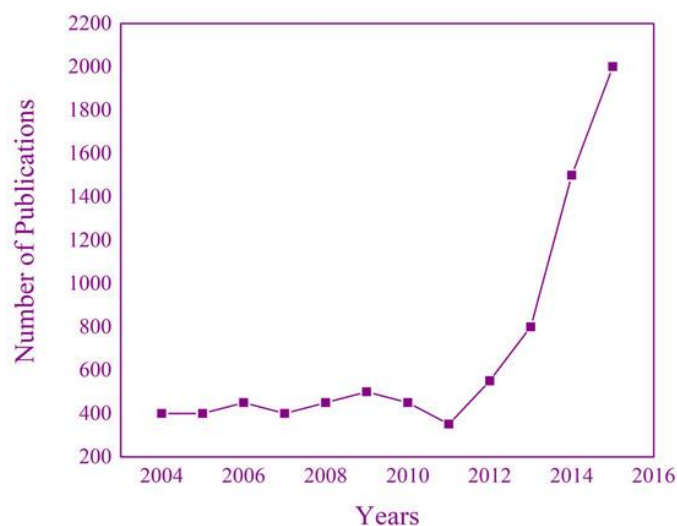


**Figure 2.3:** Chronological compilation of publications on 2D materials [25].

Two-dimensional layered materials exhibit high crystallinity and have a lateral size ranging from 1 to 10,000  $\mu\text{m}$ , while their thickness is less than 1 nm [26]. Two-dimensional materials possess a layered arrangement characterized by robust covalent bonding within each layer and comparatively feeble van der Waals interactions between the layers [27]. 2D materials possess a layered structure that enables them to exhibit efficient electrical properties. Specifically, the conductivity inside the layers is often three to four times greater than the conductivity between the layers. The identification of graphene and its distinctive characteristics in 2004 initiated a scientific upheaval [25], leading to the exfoliation of numerous other layered materials into 2D structures utilizing a combination of elements depicted in **(Figure 2.4a)**.

### 2.5.2 What are Two-Dimensional (2D) Materials?

Materials are classed based on the number of dimensions in the nano regime. For example,

- Zero-dimensional (0D) materials have all three dimensions at the nanoscale. As an example, consider nanoparticles.
- One-dimensional (1D) materials possess two dimensions in the nanoscale realm. For example, nanotubes, nanowires, and so forth.
- Two-dimensional (2D) materials are those in which just one dimension is restricted to the nano-scale range. Examples include thin films, nanosheets, and so forth.

Finally, a substance is not a nanomaterial if it has no dimensions in the nanoscale regime. We deal with these bulk commodities daily.

### 2.5.3 Why Two-Dimensional (2D) Materials?

The characteristics of materials (TMDCs, etc.) vary significantly as they transition from bulk to 2D forms. This is due to the following factors.

- **The removal of Van der Waals forces**

Bulk materials are composed of layers that are bound together by weak van der Waals forces, although they exhibit strong bonding within each layer. When an external force is applied, the weak forces between the layers break down, and the bulk material is exfoliated into separate layers. External forces include sonication, shear force, and ion intercalation, among others. Removing the weak Van der Waal forces from the material seems to significantly enhance its strength compared to its previous state. Graphene exhibits a tensile strength that is 1000 times greater than its bulk counterpart, graphite [27].

- **Increased surface-to-volume ratio**

The extent to which a material's surface area is exposed to the environment is described by its surface-to-volume ratio. In chemical processes, a larger surface area leads to more reactivity and thus quicker reaction rates. 2D materials exhibit higher reactivity compared to their bulk counterparts. As a result, 2D materials exhibit greater sensitivity to their immediate environment compared to their larger counterparts. This characteristic enables them to function as sensors.

- **Planar electron confinement**

The quantum confinement effect becomes noticeable when the particle's size is comparable to the wavelength of an electron. To properly comprehend this impact, divide the word into quantum and confinement. Confinement is the process of limiting the movement of randomly moving electrons so that their motion is confined to specific energy levels, and quantum refers to the atomic kingdom of particles. Moving down to the nano realm causes a reduction in size, which generates discrete energy levels, resulting in an increase in band gap size and energy.

#### 2.5.4 Examples of 2D materials

There are nearly hundreds of 2D materials with a wide range of qualities. Among these, intensively investigated 2D materials include:

##### **Graphene**

Graphene is a carbon lattice consisting of covalently bonded atoms arranged in a honeycomb configuration, with a thickness of just one atom. Graphene is a semi metallic material. It possesses exceptional tensile strength, elevated electric conductivity, and a high level of electron mobility [28]. Graphene has been recognized as the most robust material. Graphene is notable among other two-dimensional materials because of its distinctive characteristics, including its unique electrical band structure, high transparency with a band gap of 0 eV, and exceptional thermal conductivity ranging from 3000 to 5000  $\text{Wm}^{-1}\text{K}^{-1}$  [29]. Graphene possesses unique properties that make it a practical substitute for indium tin oxide (ITO), which is a transparent conductive oxide (TCO) frequently employed in liquid crystal displays and LEDs [30]. The flexibility of Indium Tin Oxide (ITO) was reduced due to a deficiency in flexibility and insufficient indium content. Graphene is employed in diverse domains including solar cells, energy storage devices, sensors, transistors, light detectors, and other applications [31].

##### **Hexagonal Boron Nitride (h-BN)**

h-BN exhibits a similar structural configuration to graphene, but it distinguishes itself by being an insulator with a significant band gap. Hexagonal boron nitride (h-BN) exhibits unique characteristics such as enhanced chemical durability and resistance to high temperatures. Hexagonal boron nitride (h-BN) has undergone extensive research for its diverse applications, including its use in tunnelling devices, nano-fillers, detectors, photoelectric devices, and as a wafer for graphene due to its little lattice mismatch with graphene [32].

##### **Phosphorene**

Phosphorene is a 2D material composed of a solitary layer of black phosphorous. Black phosphorus is the most stable and layered configuration of the phosphorus element. Phosphorene has emerged as a strong competitor to graphene due to the possession of a non-zero band gap. Additionally, the band gap may be adjusted by stacking varying numbers of layers, providing further flexibility. In 2014, phosphorene was initially exfoliated using mechanical exfoliation techniques [33]. Phosphorene is unstable when exposed to air and

undergoes degradation when it reacts with water vapours and oxygen species, especially in the presence of visible light. This instability is the primary drawback of phosphorene [34]. Phosphorene is used in several applications, including optoelectronic devices, inverters, transistors, and flexible circuits [35].

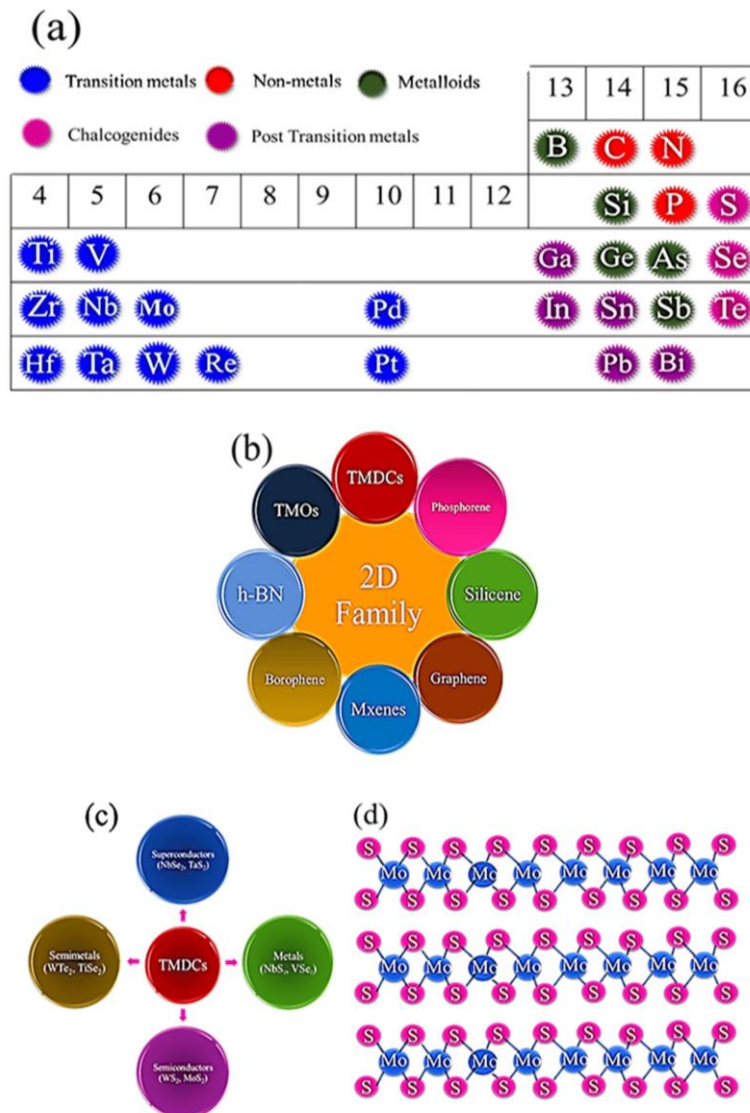


**Figure 2.4:** The 2D materials genus. (a) The most generally recognized two-dimensional layered materials are the highlighted components of the periodic table. (b,c) The Family classification of the 2D material and the Family of Transition Metal Dichalcogenides (TMDCs). (d) The generic formula of MX<sub>2</sub> in transition metal dichalcogenides (TMDCs) is consistent with the layered structure of MoS<sub>2</sub>.

## MXenes

A class of inorganic compounds in which materials contain transition metal nitrides, carbides or can contain transition metal carbonitrides are called MXenes [36]. MXenes being layered

materials, conductive, and having adjustable surface terminations enable them to play their part in applications of energy storage devices, water purification, composites, optoelectronic devices and photocatalysis etc [37].

### **Transition Metal Dichalcogenides (TMDCs)**

The expanding interest in the unique characteristics of graphene has created novel opportunities for other two-dimensional layered materials, including transition metal dichalcogenides (TMDCs), in the field of science and technology. The dominance of two-dimensional nanomaterials is attributed to their dimensionality, as well as the precise composition and arrangement of atoms in monolayers. The general formula for layered 2D transition metal dichalcogenides is  $\text{MX}_2$ , where M represents a transition metal from groups IV B, V B, VI B, or VII B (e.g., Ti, Zr, Hf, V, Nb, Ta, Mo, W, Tc, Re) and X represents a chalcogen element from group VI A (e.g., S, Se, Te). These dichalcogenides are composed of numerous crystals. **(Figure 2.4b)** depicts the overall categorization of a 2D family [38, 39]. TMDCs, or transition metal dichalcogenides, exhibit a bandgap that varies between 0 and 2 eV, subject to factors such as the presence or absence of a dopant, elemental conjunction, and layer number. Conversely, unadulterated graphene is a semimetal with a bandgap of 0 eV [40].

In addition to metals, semimetals, semiconductors, insulators, and superconductors, transition metal dichalcogenides (TMDCs) display a wide array of other features. As shown in **(Figure 2.4c)**, these characteristics are dependent on the structural architecture and elemental makeup. Layered transition metal dichalcogenides (TMDCs) are emerging as the primary contenders to replace graphene due to their transparency, flexibility, and comparable thinness to graphene [41].

The bandgap, on/off ratio, and charge carrier mobility of TMDCs are comparable to those of silicon, and they can also be stacked onto flexible substrates while still withstanding the strain and tension caused by such supports [42]. To keep their layers together, these materials use weak Van der Waals pressures acting perpendicular to the layers.

Layers of chalcogen atoms sandwich transition elements, making up TMDCs. A variety of crystal structures are exhibited by tetrahedrally coordinated metal dichalcogenides (TMDCs). Two of the most common phases are the metallic 1T phase and the semiconducting 2H phase. These materials display a controllable band gap when reduced to the nanoscale. This is because,

as the thickness or number of layers increases, their indirect band gap becomes a direct band gap.

Transition metal dichalcogenides (TMDCs) exhibit a high level of charge mobility, often ranging from 100 to 1000  $\text{cm}^2\text{V}^{-1}\text{s}^{-1}$ . This characteristic has led to their use in the development of 2-dimensional transistors. Graphene is a semimetal that does not have a band gap. In contrast, other 2D materials, specifically TMDCs, have a band gap range of 1.2 to 1.8 eV [43]. This range is well-suited for capturing solar energy and meets the requirements of the photovoltaic industry, like materials like Si (1.1 eV), CdTe (1.5 eV), or GaAs (1.4 eV). Transition metal dichalcogenides (TMDCs) have diverse uses in various disciplines including photo electronics, memory devices, lasers, field-effect transistors, photodiodes, and biological applications [27].

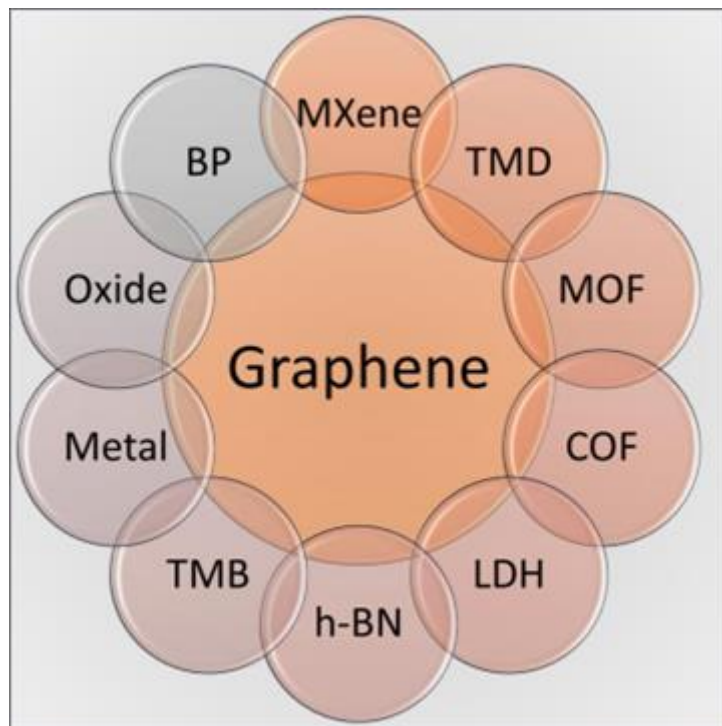


**Figure 2.5:** Examples of 2D Materials.

### 2.5.5 Bottom-up Synthesis of 2D Materials

Multiple methods exist to produce two-dimensional nanomaterials. In bottom-up methodologies, the synthesis of nanomaterials involves the initial assembly of individual atoms or molecules to form larger structures [44-46].

Bottom-up techniques in materials synthesis encompass a range of methods, such as



organic ligand aided synthesis, solvothermal synthesis, hydrothermal synthesis, polyol synthesis, templated based synthesis, photochemical synthesis, biological synthesis, wet chemical synthesis, and seeded synthesis [44-46].

The compatibility of the substrate with 2D materials has significant importance in these methodologies because of their reliance on the growing surface.

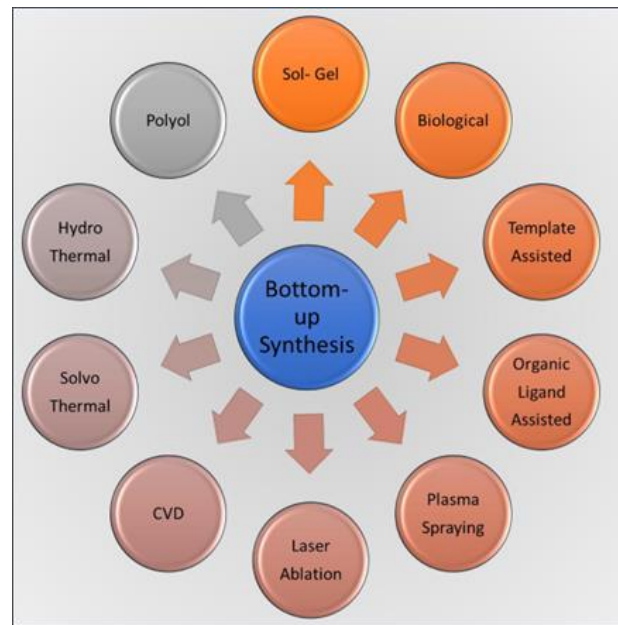


**Figure 2.6:** Bottom-Up Synthesis Methods of 2D Materials.

### 2.5.6 Top-Down synthesis of 2D Materials

Top-down methodologies encompass many techniques such as mechanical compression, nanolithography, exfoliation, micromechanical cleavage, Chemical vapor deposition, and Hummer's method [47-50].



**Figure 2.7:** Top-Down Synthesis Methods of 2D Materials.

Top-down techniques involve the initial utilization of bulk materials, which are then fragmented to provide 2D nanomaterials. The fabrication of 2D nanomaterials entails employing mechanical milling for grinding, followed by a further annealing procedure. Lithography is a viable method to produce patterned two-dimensional materials with diverse architectures. A laser beam is employed to concentrate a plasma plane within a solution after its interaction with a metal.

Sputtering is a viable method to produce thin 2D nanomaterials characterized by a monolayer or a limited number of layers. Thermal breakdown causes the separation of chemical bonds in the compounds, leading to the creation of two-dimensional (2D) materials [51, 52].

## 2.6 Molybdenum Disulphide

Molybdenum disulfide ( $\text{MoS}_2$ ) is a prominent constituent of the transition metal dichalcogenides (TMDs), renowned for its stratified configuration and versatile characteristics [53]. Consequently, it has garnered significant attention and investigation in various scientific and industrial fields.  $\text{MoS}_2$  consists of a monolayer of molybdenum (Mo) atoms sandwiched between two monolayers of sulfur (S) atoms. This configuration creates a three-layered structure with robust covalent connections inside each layer and less powerful van der Waals forces between the layers.  $\text{MoS}_2$  may be readily exfoliated into thin sheets due to its distinctive structure, resulting in a significant improvement in its surface properties [54].

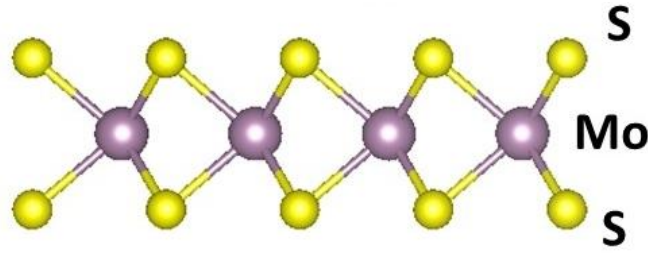


**Figure 2.8:** MoS<sub>2</sub> structure showing Mo sandwiches between two sulfur atom layers.

### 2.6.1 Properties of MoS<sub>2</sub>

Molybdenum disulfide (MoS<sub>2</sub>) is a material that is highly adaptable and possesses a wide range of extraordinary properties, making it suitable for a wide range of applications. The properties can be classified into structural, electrical, optical, mechanical, thermal, and chemical properties [55].

- **Bandgap:** The bandgap of MoS<sub>2</sub> varies depending on its thickness. The indirect bandgap of MoS<sub>2</sub> is approximately 1.2 eV in the bulk form, while the direct bandgap of MoS<sub>2</sub> is approximately 1.8 eV in the monolayer form [56]. The transition from an indirect to a direct bandgap enhances its optical and electrical capabilities.
- **Electric charge Monolayer:** MoS<sub>2</sub> possesses a high level of carrier mobility, rendering it well-suited for utilization in electrical devices including transistors and sensors. The range of typical carrier mobility values is between 10 and 200 cm<sup>2</sup>/V·s, which varies based on the quality and production procedure.
- **Flexibility and Strength:** MoS<sub>2</sub> nanosheets exhibit an extraordinary tensile strength and a high Young's modulus of approximately 270 GPa. These characteristics render them pliable and robust, rendering them well-suited for the use in nanomechanical devices and flexible electronics.
- **Durability:** The layers' strong covalent bonding enhances its mechanical strength.
- **Thermal Stability:** MoS<sub>2</sub> has excellent stability at elevated temperatures, undergoing breakdown only at around 1100°C in atmospheres devoid of reactive substances. This feature renders it appropriate for high-temperature applications.
- **Chemically inert:** MoS<sub>2</sub> exhibits chemical inertness, meaning it is unreactive and does not undergo oxidation or corrosion when exposed to normal environmental conditions. This improves its resilience and longevity in a wide range of uses.

- **Large Surface Area:** The presence of numerous active sites for interactions is the consequence of the high surface area of MoS<sub>2</sub> when it is transformed into nanosheets. This characteristic is advantageous for various applications, including adsorption and catalysis.
- **Photoluminescence:** Monolayer MoS<sub>2</sub> displays strong photoluminescence due to its straight bandgap, rendering it extremely advantageous for optoelectronic applications such as LEDs and photodetectors.
- **Absorption Spectrum:** MoS<sub>2</sub> displays a prominent absorption spectrum in the visible range, making it advantageous for utilisation in solar cells and photodetectors.

### 2.6.2 Application of MoS<sub>2</sub>

Due to its unique properties, MoS<sub>2</sub> has a wide range of uses. MoS<sub>2</sub> is employed in field-effect transistors (FETs) in electronics because of its exceptional electron mobility and direct bandgap, which significantly enhances the performance of electronic circuits [57]. Furthermore, its sensitivity to changes in the environment makes it very suitable for gas and chemical sensors. The strong light absorption and photoluminescence properties of MoS<sub>2</sub> are utilized in optoelectronic photodetectors to efficiently convert light into electrical signals. The material's direct bandgap is advantageous for LEDs as it enables efficient light emission. Additionally, it improves the ability of solar cells to absorb light and convert it into electricity.

The catalytic properties of MoS<sub>2</sub> are crucial in the hydrogen evolution reaction (HER), as it effectively produces hydrogen by dividing water [58]. Moreover, it is widely used in hydrodesulfurization to effectively remove sulphur from petroleum products, which is a crucial step in the manufacturing of environmentally friendly fuels. The high surface area and electrical conductivity of MoS<sub>2</sub> enhance the performance of electrodes in lithium-ion and sodium-ion batteries, as well as in supercapacitors that require fast charge-discharge cycles, hence boosting energy storage [59].

MoS<sub>2</sub> is employed in environmental applications, specifically in dye adsorption, where its nanosheets effectively remove colour molecules from wastewater [60]. The enormous surface area and active adsorption sites of the nanosheets considerably help water filtration efforts. Furthermore, MoS<sub>2</sub> possesses the capability to function as a catalyst for the breakdown of pollutants in water, thereby aiding in environmental rehabilitation endeavors. The mechanical

strength and flexibility of MoS<sub>2</sub> make it highly suitable for flexible electronics, enabling the development of bendable and wearable devices such as flexible displays and sensors. When it comes to lubricants, bulk MoS<sub>2</sub> is an outstanding solid lubricant since it has a low friction coefficient and is highly stable at high temperatures. It efficiently minimizes wear and friction in mechanical systems [61].

## 2.7 Role of Nanotechnology in Wastewater Treatment

Conventional methods of water treatment are inadequate for effectively eliminating pollutants. These methods are not sufficiently effective in meeting the stringent standards for water quality. There is a pressing demand for more powerful and efficient solutions to manage both industrial and community wastewater. Among other technological tools, the emergence of nano technology has shown great potential for wastewater treatment. Nanotechnology has contributed to water remediation by many means, such as nano-adsorbents, membranes, nano-catalysts, and nano composites. Recent literature has extensively shown the use of nano-adsorbents for effectively removing pollutants [62-66].

**Table 2.1:** List of Adsorbents (MoS<sub>2</sub> and Cu-MOF) for Adsorption of Organic Dye Reports in Recent Years

Sr. No.	Adsorbent	Adsorbate	Year of Publication	Reference
1.	MoS <sub>2</sub> decorated with magnetic Fe <sub>2</sub> O <sub>3</sub> NPs	CR	2015	[67]
2.	Hierarchical MoS <sub>2</sub> -NS microspheres	MB	2016	[68]
3.	Cu-BTC@GO Cy-BTC@CNT Fe <sub>3</sub> O <sub>4</sub> / Cu-BTC@GO	MB	2016	[69]

4.	MoS <sub>2</sub> Nano-sheets	MB MG Rh CR	2016	[70]
5.	MoS <sub>2</sub> @rGO Nano composite	CR	2017	[71]
6.	Flower-Like MoS <sub>2</sub> Nanostructure	RhB MB	2017	[72]
7.	Fe <sub>3</sub> O <sub>4</sub> / Cu-BTC	Malachite green	2018	[73]
8.	MoS <sub>2</sub> microspheres	MO	2019	[74]
9.	Cu-BTC	MB	2019	[75]
10.	Hierarchical MoS <sub>2</sub> microspheres	RhB	2019	[76]
11.	MOFs	AO7	2019	[77]
12.	Meso-porous C/MoS <sub>2</sub>	MO	2020	[78]
13.	MoS <sub>2</sub> @ZIF-67	MO	2023	[79]
14.	MoS <sub>2</sub> @Cu-MOF	MB	-----	-----

## 2.8 Adsorption Study

### 2.8.1 Background

The leading causes of water shortage are industrial, urban, and agricultural pollution. From available freshwater resources, the utilization of water in these sections is 70% for agricultural, 22% for industrial and 8% for domestic use and accordingly a great quantity of wastewater,

carrying a diversity of pollutants, has been produced [80]. Undoubtedly, the discharge of wastewater from industrial and commercial sectors introduces harmful pollutants into freshwater reservoirs, posing a catastrophic threat to not only human society but also to animals, plants, and the ecosystem. The presence of dominant water contaminants such as oils, heavy metal ions, and organic wastes (specifically dyes) in any cascade renders it unfit for consumption [81].

For millennia, dyes have been effectively utilized in several industries including food, paint, cloth, paper, pigment, cosmetics, and more. Currently, a total of 100,000 distinct varieties of dyes have been manufactured and made available for commercial purposes. In terms of use, a total of 1.6 million tons of different dyes are used on a yearly basis. Therefore, around 10-15% of colors are lost during usage [82]. Azo dyes exhibit resistance and tolerance to aerobic digestion and oxidizing environments, distinguishing them from other types of colors. The existence of several benzene rings in azo dyes is responsible for all of this. Globally, approximately 1-20% of the total dye production is lost in industrial wastewater according to statistics. The dispersion of vibrant waste materials into water impedes the penetration of sunlight, hence hindering the photosynthetic activity of aquatic plants and algae [83]. Furthermore, azo dyes have been scientifically demonstrated to have a negative impact on the metabolites of both humans and animals due to their mutagenic, poisonous, and carcinogenic properties [84].

The critical problem of water contamination has prompted the examination of numerous potential solutions. The primary methods that have been assessed in this area are coagulation, adsorption, flocculation, ion-exchange, biodegradation, and oxidation [85, 86]. Each approach has its own advantages and disadvantages. Adsorption has been extensively employed due to its remarkable efficiency, ease of operation, diversity, low energy consumption, and cost-effectiveness [87].

### 2.8.2 Adsorption Isotherms

A proper understanding of the adsorption isotherms is required to accurately interpret the mechanism of adsorption process and for successful adsorption system-design. In present time, linear regression model is the most implemented tool for defining and elucidating the prime fitting model for adsorption [88]. The process of pigment adsorption was analyzed using two

adsorption isotherms: the Freundlich adsorption isotherm and the Langmuir adsorption isotherm.

### Langmuir Adsorption Isotherm

In the Langmuir model, it is assumed that the adsorbent surface is composed of a single molecule at the point of maximal coverage. It means that only one dye molecule gets adsorbed at one adsorption active site of adsorbent and generates monolayer. This indicates that dye molecules are not piled up on the adsorbent surface [89-93]. The Langmuir adsorption isotherm can be represented by the following expression:

$$\frac{C_e}{Q_e} = \frac{1}{Q_M K_L} + \frac{C_E}{Q_M}$$

Where:

C<sub>e</sub>= the concentration of the adsorbate at equilibrium (mg/L)

Q<sub>e</sub>= the amount of MB dye adsorbed per gram of adsorbent (mg/g)

Q<sub>m</sub>= Maximum capacity of monolayer coverage (mg/g)

K<sub>L</sub>= Langmuir isotherm constant (L/mg)

The following equation expresses the basic features of the Langmuir isotherm in terms of a dimensionless constant separation factor R<sub>L</sub>

$$R_L = \frac{1}{(1 + K_L C_0)}$$

Where C<sub>0</sub> is the highest initial concentration of adsorbate (mg/L).

The R<sub>L</sub> value indicates that the isotherm's shape is either unfavorable (R<sub>L</sub>> 1), linear (R<sub>L</sub> = 1), favorable (0 <R<sub>L</sub> <1), or irreversible (R<sub>L</sub> = 0).

### Freundlich Model Isotherm



The empirical equation used to characterize systems with heterogeneity is the Freundlich isotherm. Here is the equation that defines this model [89-94]:

$$Q_e = K_F C_e^{1/n}$$

This equation, in its linear version, is expressed as \*\*:

$$\ln Q_e = \frac{1}{n} \ln C_e + \ln K_F$$

$K_F$  and  $n$  are Freundlich constants.  $K_F$  is a crude indicator of the sorbent's adsorption capacity, while  $n$  indicates the adsorption process's favorable direction. The adsorption favorability is indicated by the exponent's magnitude,  $1/n$ . A normal adsorption is indicated by a value of  $1/n$  that is less than 1. A favorable sorption process is indicated when  $n$  falls within the range of one to ten\*\*.

With an increase in temperature, the values of the constants  $K$  and  $n$  adjust to accurately represent the empirical finding that the amount of adsorption grows at a slower rate and higher pressures are needed to fully saturate the surface\*.

### 2.8.3 Adsorption Kinetics

The investigation of adsorption kinetics is significant since it offers essential understanding into the progression and mechanism of processes. The adsorption rate was investigated by studying the contact time for a duration of up to 6 hours and then compared to theoretical models. In this study, the researchers assessed pseudo first-order and second-order kinetic models using experimental data gathered for various contact times.

The pseudo first-order equation (Lagergren equation) is employed to ascertain the rate constant for the adsorption of adsorbate from the effluent onto the adsorbent [89, 90]:

$$\log(Q_e - Q_t) = \log Q_e - \left(\frac{K_1}{2.303}\right) t$$

The adsorbent's adsorption capacity at equilibrium is given by  $Q_e$  (mg/g), the amount of dye absorbed at time  $t$  is given by  $Q_t$  (mg/g), and  $K_1$  is the pseudo first order rate constant ( $\text{min}^{-1}$ ). The integrated second order rate law can be used to express the pseudo second order kinetics in a linear form.

$$\frac{t}{Q_t} = \frac{1}{Q_e} t + \frac{1}{K_2 Q_e^2}$$

$K_2$  is the rate constant for a pseudo second order reaction, measured in units of  $\text{g mg}^{-1} \text{min}^{-1}$ .

A pseudo second-order model indicates that the adsorption process is influenced by both the adsorbate and the adsorbent and involves a combination of chemisorption and physisorption. Chemisorption could potentially be the step that limits the rate of a reaction, in which valence forces play a role through the sharing or exchange of electrons between the adsorbent and the adsorbate [95, 96].

## CHAPTER 3: MATERIALS AND METHODS

### 3.1 Materials and Chemicals Utilized

Analytical-class materials and chemicals were all needed for the synthesis of the samples, and no further purification step was necessary.

- Copper nitrate trihydrate ( $\text{Cu}(\text{NO}_3)_2$ ) Merck, Germany
- 1,3,5-benzene tricarboxylic acid (BTC) Panreac
- N-Methyl-2-pyrrolidone (NMP) EMPLURA
- Molybdenum disulfide powder ( $\text{MoS}_2$ ) Sigma Aldrich
- Methylene Blue
- Ethanol ACL Labscan
- DI Water

### 3.2 Methodology

#### 3.2.1 Synthesis of Cu MOF (HKUST-1, Cu-BTC OR MOF-119)

The Cu-MOF was synthesized using a previously disclosed process, with minimal modifications to the parameters [97]. 1.522g of Cu Nitrate was added in 22.5ml of DI water and stirred for 10 minutes. 0.567g of BTC was added in 22.5ml of NMP and Ethanol solution (1:1), stirred for 10 minutes. The prepared solutions were combined and transferred to a stainless-steel jar lined with Teflon. The mixture was then heated at a temperature of 120°C for a duration of 24 hours. Once the reaction had finished, the vessel was cooled to the surrounding temperature. The resulting Cu-MOF was then washed with ethanol and subsequently with DI water, using vacuum filtering. The sample obtained was dried at 60°C (overnight) in vacuum oven. The dried sample was collected and stored.

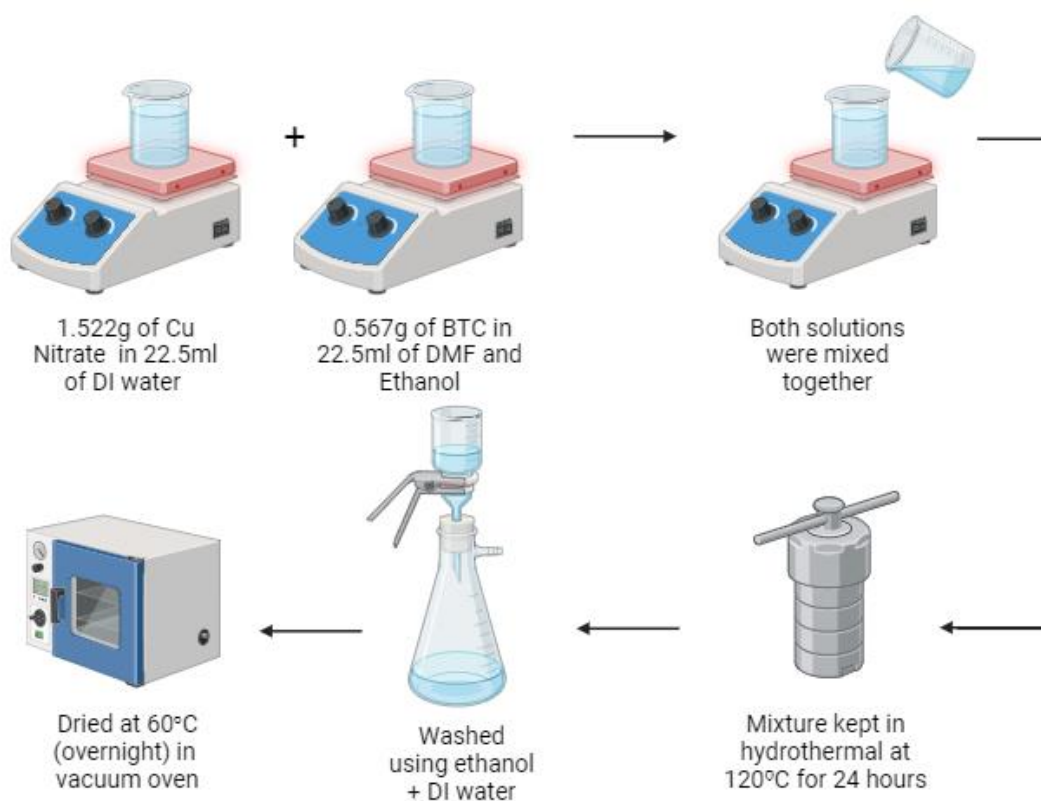


**Figure 3.1:** Schematics of Cu-MOF synthesis

**Figure 3.2:** Schematics of Chemical Exfoliation of Bulk MoS<sub>2</sub> by Adding Liquid Nitrogen

### 3.2.2 Exfoliation of Bulk MoS<sub>2</sub> by Probe Sonication Method

The exfoliation of MoS<sub>2</sub> was conducted using a previously documented technique, with certain adjustments [98]. 300mg MoS<sub>2</sub> was added in 40 ml NMP in a metallic beaker. The mixture was subjected to Probe sonication followed by cold water bath at 130W (20% power) for 10 hours with on 7s and off 1s. To separate the thick sheets, the mixture was centrifuged at 700 rpm. After centrifuging at 500 rpm for 30 minutes, the remaining contents of the tube were sonicated in a bath for 5 minutes. After allowing the collected supernatant to dry overnight, the nanosheets were ground, scraped, and finally collected.

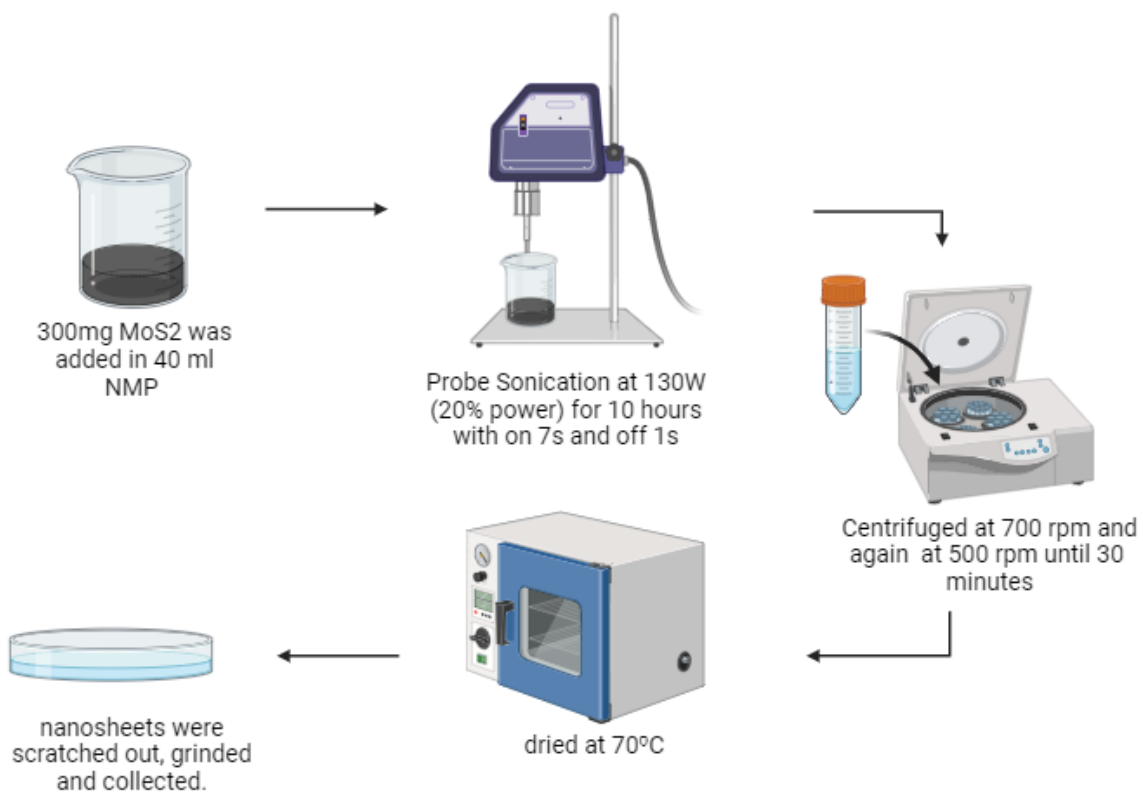


**Figure 3.2:** Schematics of Bulk MoS<sub>2</sub> by Probe Sonication Method

### 3.2.3 In-Situ Synthesis of Exfoliated MoS<sub>2</sub>/Cu-MOF Nanocomposite

The desired composite was synthesized according to a previously published method, with slight change of parameters [79]. 0.089g MoS<sub>2</sub> nanosheets were dissolved in 1.522g Cu-Nitrate in 11.25 ml of DI water which was stirred for 20 min. Mix 11.25 milliliters of ethanol and DMF with 0.56g of BTC and mix for 10 minutes. A stainless-steel container lined with Teflon was used to heat the solutions for 24 hours at 120°C. Following the completion of the reaction, the vessel was cooled to room temperature. The resulting Cu-MOF was subsequently cleaned with ethanol and DI water using vacuum filtering. Overnight in a vacuum oven, the collected sample was dried at 60°C. The sample was taken and kept after drying. Table 3.1: Experimental conditions for several synthesized samples

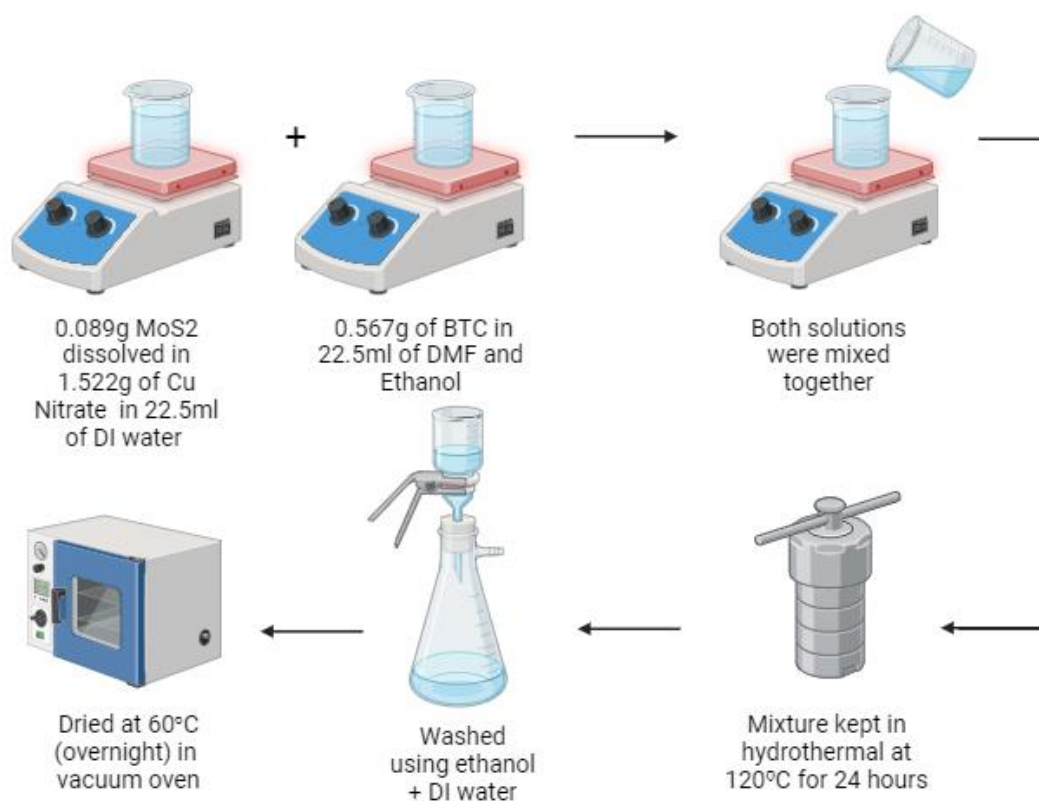


**Figure 3.3:** Schematics of Exfoliated MoS<sub>2</sub>@Cu-MOF Nanocomposite synthesis

**Table 3.01:** Experimental conditions for several synthesized samples

Sr. No.	Sample	Methodology	Experimental Conditions
1	Cu-MOF	Hydrothermal	24 hours mixing of precursors at Hydrothermally
2	MoS <sub>2</sub> nanosheets	Exfoliation using Probe Sonication	Sonicated at 130W (20% power) for 10 hours with on 7s and off 1s.

3	9% Exfoliated MoS <sub>2</sub> /Cu-MOF nanocomposite	In-Situ strategy	<p>0.089g MoS<sub>2</sub> added in 1.522g Cu-Nitrate dissolved in 11.25 ml DI water.</p> <p>0.56g of BTC in 11.25 ml of ethanol and DMF.</p> <p>Both were mixed and transferred to Teflon lined vessel and placed in hydrothermal for 24hrs at 120°C.</p> <p>The obtained product was washed and dried.</p>
---	--	------------------	---

## CHAPTER 4: CHARACTERIZATION

### 4.1 Instruments

The synthesized Cu-MOF and 2D MoS<sub>2</sub> samples were examined using a variety of analytical techniques, including atomic force microscopy (AFM), scanning electron microscopy (SEM), X-ray diffraction (XRD), Fourier transform infrared spectroscopy (FTIR), RAMAN, and UV-visible spectroscopy.

### 4.2 SEM

This approach involves the precise focusing of a narrow electron beam onto the surface of an object. As a consequence, particles such as photons or electrons are dislodged from the surface of the material. Subsequently, the dislodged electrons are directed into the detector for further analysis. The signal generated by the detector causes variations in the luminosity of the cathode ray tube (CRT). The material's image is generated by plotting a corresponding point on the cathode ray tube (CRT) at each interaction site between the beams [99].

When electrons come into contact with surfaces, they produce emissions such as backscattered electrons (BSE), X-rays, and secondary electrons (SE) [100]. Secondary electrons are the predominant method of detection in scanning electron microscopy (SEM). The emission of these electrons occurs in close proximity to the surface of the sample, acquiring a distinct and lucid representation of the specimen.

The technique has the capability to discern minute features with dimensions less than 1 nanometer. Moreover, the phenomenon of elastic scattering occurs when input electrons interact with a target material, resulting in the emission of backscattered electrons. Secondary electrons are found at shallower depths compared to primary electrons. The resolution of the given entity is somewhat lower in comparison. When an electron located in the inner shell is dislodged from its orbit, it releases x-rays that possess distinct characteristics [101].

The utilization of scanning electron microscopy (SEM) is favored due to its convenient sample preparation methods, enabling researchers to examine several aspects of a sample, including its morphology, chemistry, crystallography, and orientation of planes. The scanning electron microscope (SEM) has a variable magnification range spanning from 10 to 500,000 times. The morphology of the materials can be investigated using the any instrument, and better resolution can be obtained using FESEM. The elemental composition can be ascertained using an A Field Emission Scanning Electron Microscope (FESEM) attached to an Energy Dispersive X-ray Spectroscopy (EDS) detector.



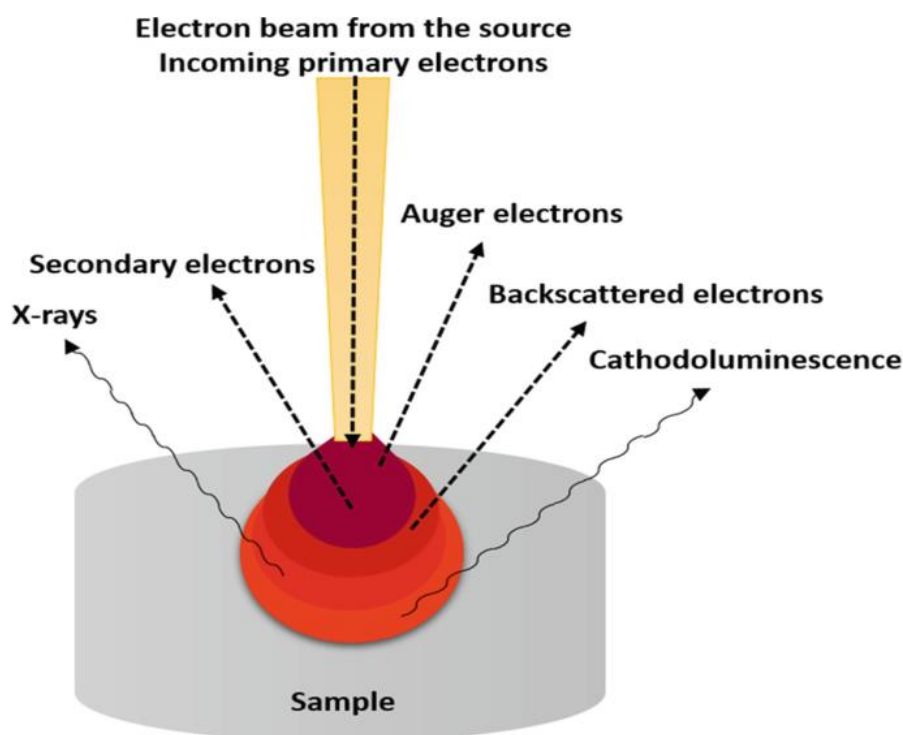


**Figure 4.1:** Interaction between an electron beam and a specimen

#### 4.2.1 Sample Preparation

In order to characterize the nano particles, the specimens underwent a drying process in a drying oven that was kept at a constant temperature of 60°C for a period of 3 hours. The samples were finely ground after drying to get accurate results.

A conductive gold coating with a thickness of a few nanometers was applied onto a two-dimensional (2D) MoS<sub>2</sub> and Cu-MOF to enhance the conductivity of the surface and enable high-resolution imaging. Subsequently, the specimens were subjected to analysis at several levels of magnification, and the most optimal photographs exhibiting superior resolution were captured.

### 4.3 XRD

A nondestructive method that can be used to identify residual stresses, elastic characteristics, and the identity of unknown materials in the lattice spacing of crystalline solids. Lattice spacing is calculated when x-rays with a known wavelength and angle enter a material, travel through atomic planes, and then refracted through to a diffractometer to measure

intensity. In order to properly identify the planes present, X-rays are directed toward the sample at various angles to activate the planes at those distinct angles. It is common practice to identify the atomic spacing and Miller indices (hkl) of a powder sample by subjecting it to X-ray radiation. The measured intensities correlate to particular elements or phases. The sample exhibits several intensity peaks, indicating the presence of multiple constituents or phases [102].

A heated filament's electrons hit a copper target material, displacing the electrons in its inner shell, and causing X-rays to be released. The X-rays that are produced are directed and concentrated onto the sample using collimation, where they deflect back to satisfy Brag's law:

$$2d\sin\theta = n\lambda$$

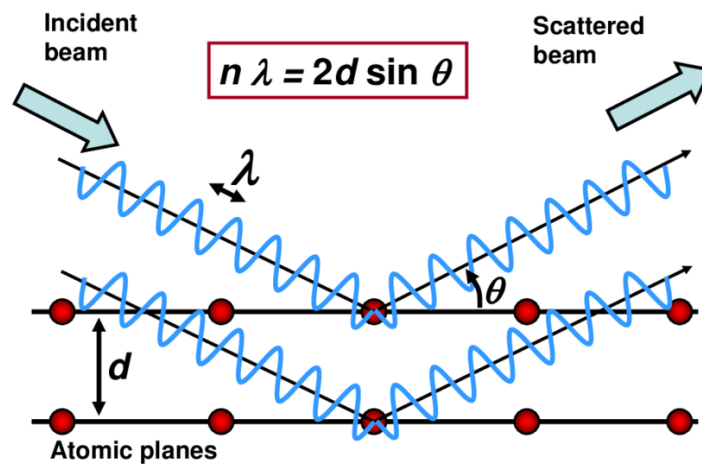


**Figure 4.2:** Mechanism of action of X-ray diffraction (XRD).

A diffractometer then records the X-ray signals, turning them into counts (peaks) that are displayed on a computer screen.

The orientation of the various crystalline phases that are present can be determined using X-ray diffraction. It is also utilized for measuring the thickness of thin films and multilayer materials, as well as for determining structural factors such as strain, atomic arrangement, lattice parameters, and phase composition.

#### 4.3.1 Sample Preparation

The X-ray diffractometer (Bruker D2 PHSER diffractometer) was employed to investigate the crystal structure and, notably, to examine the arrangement of 2D MoS<sub>2</sub> sheets and Cu-MOF along a designated plane. The X-ray diffraction (XRD) analysis provided confirmation of the existence of well-formed two-dimensional (2D) MoS<sub>2</sub> structures, with their orientation aligned parallel to the plane. The samples were analysis using two distinct methodologies in X-ray diffraction (XRD).

For XRD analysis, a preliminary preheating or drying step is performed in a drying oven at a temperature of 60 °C for a period of 3 hours. This step was conducted to eliminate any moisture that may have been present or trapped inside the layers of the sample. Subsequently, the desiccated samples were immediately transferred to the stub or sample holder of the X-ray diffraction (XRD) instrument for examination.

The samples were analysis at a range of angles spanning from 0° to 80°, utilizing a slow scan rate for structure and phase identification.

#### 4.4 FTIR

It is a physio chemical spectroscopic technique which helps in determining the functional groups of organic and non-organic compounds by determining their vibrations. When the n material is exposed to IR radiation, the molecules in it get excited and show different vibrations in different frequency ranges. In case of composites, FTIR helps in determining the presence of fillers as well as chemical bonding of materials. In electromagnetic spectrum, infrared region lies in the range of (14000-10) cm<sup>-1</sup> and can be further divided as:

- The near-infrared (IR) range spans from 400 to 10 cm<sup>-1</sup>.
- The mid-infrared (IR) range covers 4000 to 400 cm<sup>-1</sup>.
- The far-infrared (IR) range extends from 14000 to 4000 cm<sup>-1</sup>.

The mid-infrared (IR) area is commonly referred to as the finger-print region. The IR active molecules show their characteristic primary vibrations in this region which ultimately helps in determining/identifying the functional groups.

In this technique, the analyte is exposed to the range of wavelengths and the molecular bonds show absorbance at specific wavelengths undergoing excitation which further leads to vibrations. These vibrations could be stretching and bending. Bending vibrations are also called

contractions. The IR spectrum is plotted between wave numbers on X-axis while absorbance or transmittance on Y-axis. It follows Beer-Lambert law,

$$A = \epsilon.C.l$$

Where, A= absorbance,  $\epsilon$  = molar absorptivity, C= concentration, l = path length.

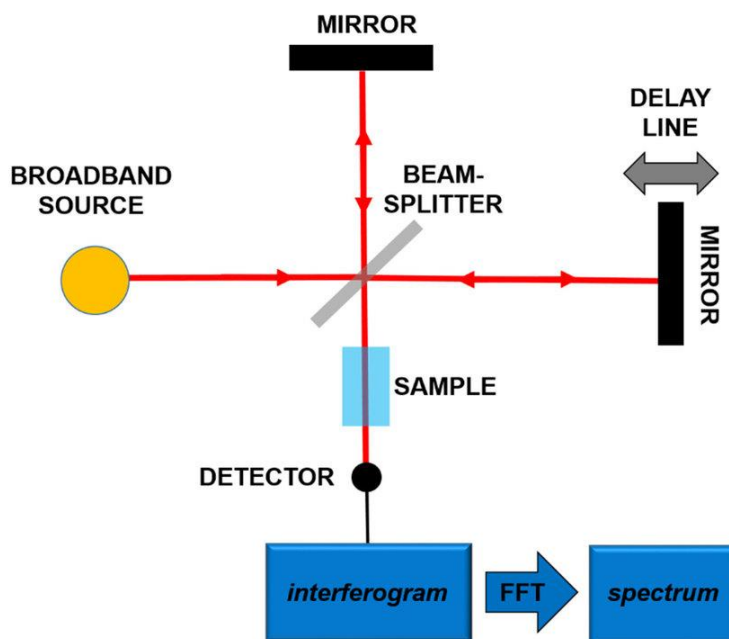


**Figure 4.3:** Illustration of the functioning of FTIR spectroscopy

#### 4.4.1 Sample Preparation

Typically, samples are made by mixing nanoparticles with potassium bromide (KBr), in which KBr is in more amount in comparison to the nanoparticles and then crushing the mixture into a pellet using a uniaxial press. This pellet is then utilized for characterization.

### 4.5 Raman Spectroscopy

A Raman Spectrometer is a device that uses lenses and filters to concentrate light from a single or several colored sources, distinguish between reflected and dispersed light, and measure the intensity of each. In order to separate light into its component parts, a prism is utilized. These parts contain a detector that can detect faint light. Afterwards, the spectrum is displayed on the screen for analysis.

Radiation can be reflected, absorbed, or dispersed when monochromatic light is passed through a substance; this is the fundamental principle underpinning Raman spectroscopy. Due

to differences in vibrational and rotational properties, the incident and dispersed photons have different frequencies. Infrared spectra are used to study the resulting wavelength change.

One measure of dispersion between incident and scattered photons is the Raman shift. When scattered photons have an energy lower than the incident photons, this phenomenon is called Stokes scattering. When the scattered photons' energies are higher than the incident photons' energies, this process is called anti-Stokes scattering.

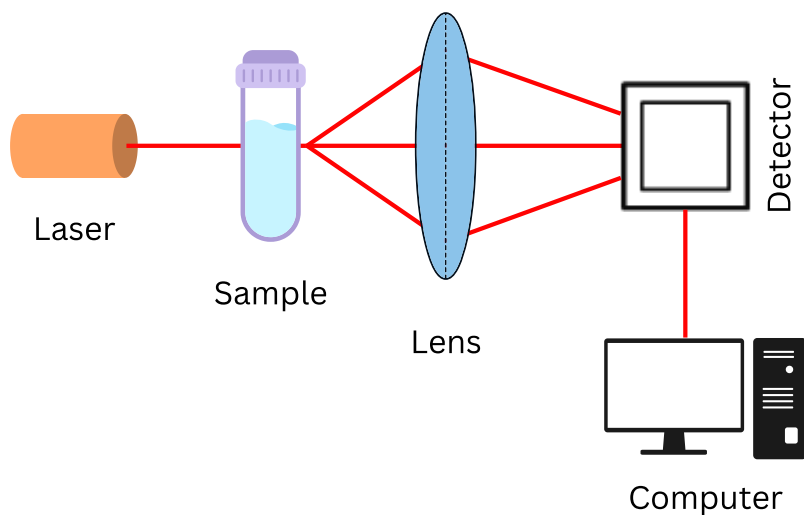


**Figure 4.4:** Assembly of the Raman spectroscopy

The Raman effect is analyzed by converting the wavelength of the scattered photon to a wavenumber. The x-y plane is used to plot these wavenumbers. The Raman intensity is measured on the y-axis, while the wavenumbers are measured along the x-axis. The disparity between intensity and wavenumbers is referred to as the Raman spectrum.

#### 4.5.1 Sample Preparation

Preparing solid samples for Raman spectroscopy involves several meticulous steps to ensure that the sample is suitable for analysis and that the resulting Raman signal is of high quality. The initial step in the process is to sanitize the sample surface to eliminate any contaminants that could potentially disrupt the Raman signal. This frequently entails employing suitable solvents or cleaning techniques to eradicate dust, oils, or residues. To boost uniformity and improve the Raman signal of crystalline or heterogeneous solid samples, it is beneficial to grind them into a fine powder. On the other hand, for reflecting or smooth samples, achieving a clean surface may need polishing. Once cleaned and, if necessary, ground, or

polished, the sample is then mounted on a suitable holder or substrate, such as a glass slide or metal plate. It is crucial to ensure that the sample is securely fixed and correctly positioned for laser excitation. By following these steps, the sample can be optimally prepared for Raman spectroscopy, ensuring accurate and reliable results.

#### 4.6 AFM

AFM is widely regarded as a very sophisticated methodology employed for examination and characterization of surfaces. This technique is mostly employed for the purpose of assessing surface roughness and analyzing characteristics at the micro and nano scales. The utilization of 2D materials allows for an approximate determination of the dimensions of the sheet, including its length and thickness [103].

The fundamental idea behind atomic force microscopy (AFM) is the interaction between a sharp cantilever, which is spring-based, and the surface of the specimen [104]. The measurement of force is conducted by observing the deflection of the specimen during scanning. Another rationale for employing atomic force microscopy to analyze exfoliated sheets was to assess the aspect ratio (length/thickness), which has significant relevance in subsequent modeling endeavors aimed at investigating gas barrier features.

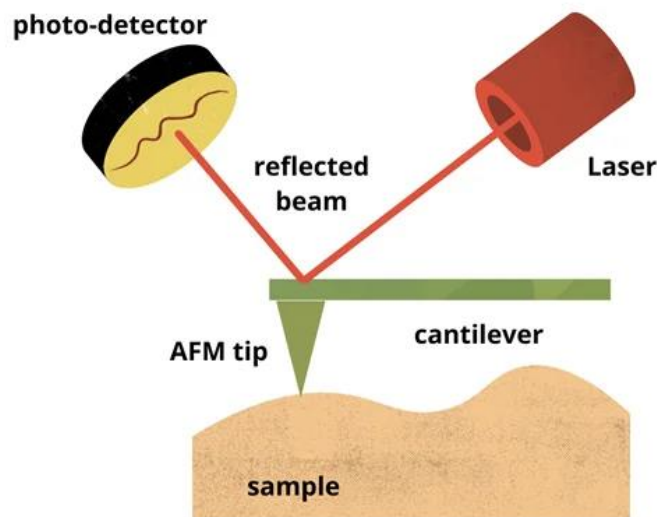


**Figure 4.5:** The AFM principle

#### 4.6.1 Sample Preparation

Atomic forces were employed to generate a three-dimensional picture. The utilization of AFM in contact mode characterized by its high-resolution capabilities, enables the determination of sheet thickness.

A dispersion preparation was conducted by adding 2D MoS<sub>2</sub> in deionized water (DIW) and subjecting it to ultrasonication at room temperature for a duration of 1 hour. A single droplet of the produced dispersion was applied over a smooth and polished Si/SiO<sub>2</sub> surface, which exhibited little roughness. For the desiccation process, the specimen was placed in a vacuum oven and heated to 70 °C for four hours. After that, the treated samples were placed in a vacuum and scanned one by one with an AFM.

#### 4.7 UV-Vis Spectroscopy

Spectroscopy involves measuring and interpreting the emission or absorption of electromagnetic radiation as ions, molecules, or atoms change energy levels. As a type of absorption spectroscopy, ultraviolet (UV) spectroscopy examines how molecules absorb light in the ultra-violet range (200-400 nm). Electrons are excited when they undergo this process of absorption, which elevates them from their ground state, their lowest energy level.

Light and matter interaction is the main focus of spectroscopy. The process by which atoms or molecules in materials absorb light results in an increase in their energy levels. A process known as excitation occurs when electrons are excited from their lowest energy state to a higher energy state because of ultraviolet radiation absorption.

Molecules containing  $\pi$ -electrons or nonbonding electrons (n-electrons) can absorb ultraviolet light, which causes these electrons to move to higher anti-bonding molecular orbitals. Electrons can absorb light with longer wavelengths more readily when they are more susceptible to being stimulated. The four types of transitions ( $\pi$ - $\pi^*$ , n- $\pi^*$ ,  $\sigma$ - $\sigma^*$ , and n- $\sigma^*$ ) can be ordered in the following sequence:  $\sigma$ - $\sigma^*$  > n- $\sigma^*$  >  $\pi$ - $\sigma^*$  > n- $\pi^*$ . Chemical molecules exhibit a distinctive spectrum when they absorb ultraviolet (UV) light, which can be employed for the purpose of identification [105].

The Beer-Lambert Law states that the absorbance is directly proportional to the concentration of the chemical in solution, making it possible to use UV-visible spectroscopy to measure the concentration of a sample. It is possible to put the Beer-Lambert Law into equation form:

$$A = \epsilon Lc$$

Where

A = absorbance

L = The optical path length, which is the measurement of the dimension of the cell or cuvette (cm).

c = The concentration of the solution (mol dm<sup>-3</sup>).

$\epsilon$  = The constant  $\epsilon$ , which is defined as molar extinction at a given wavelength (dm<sup>3</sup> mol<sup>-1</sup> cm<sup>-1</sup>), is specific to a given substance.

By measuring and plotting the absorbance of a succession of sample solutions with known concentrations against their corresponding concentrations, the Beer-Lambert Law states that the absorbance versus concentration plot should be linear.

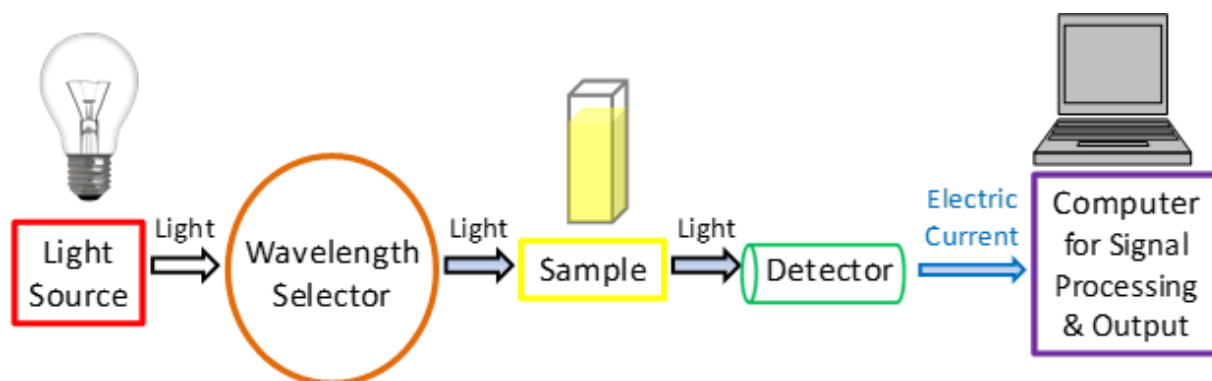


**Figure 4.6:** A demonstration of the principle of UV spectroscopy

#### 4.7.1 Sample Preparation

All the samples were diluted in deionized water with a solute to solvent ratio of 1 mg per milliliter in order to characterize the nanoparticles. The material was poured into quartz cuvettes, which were utilized to characterize the sample in the 400–700 nm range.

When data for path length, absorbance, and molar absorptivity are known, Beer-Lambert's can be used to calculate the sample's concentration in mol L<sup>-1</sup>.



## CHAPTER 5: RESULTS AND DISCUSSION

### 5.1 Scanning Electron Microscopy

Scanning electron microscopy (SEM) was used to analyze the surface morphological examinations of the as-synthesized samples. Fig 5.1 demonstrates the morphological characteristics of Cu MOF, Bulk MoS<sub>2</sub>, MoS<sub>2</sub> Nanosheets and Cu-MOF/MoS<sub>2</sub> nanocomposite. Figure 5.1 (A) and (B) clearly illustrates the porous octahedral structure of the Cu MOF crystals. The Cu MOF samples had crystal sizes from 5 to 10  $\mu\text{m}$ , exhibiting no evidence of aggregation. The morphology of the Cu MOF samples in their original form displayed a structure like the SEM images previously reported for this material [106].

Figure (C) presents SEM images of bulk MoS<sub>2</sub>, distinguished by stacked layers with micrometer-scale thickness. The layers are densely compacted, signifying the conventional structure of bulk material. Conversely, Figures (D) and (E) illustrate exfoliated MoS<sub>2</sub> nanosheets, whereby the liquid exfoliation method has successfully separated the layers, yielding a more scattered and thinner configuration. The exfoliated nanosheets have markedly decreased thickness and enhanced surface area relative to the bulk material. The photos validate the efficacy of the exfoliation procedure in converting bulk MoS<sub>2</sub> into few-layer or monolayer nanosheets [107, 108].

The SEM images of the Cu-MOF/MoS<sub>2</sub> sheets in Figures (F) and (G) demonstrate the effective integration of both materials, showcasing unique morphological characteristics. The Cu-MOF has a crystalline, porous architecture, whereas the MoS<sub>2</sub> sheets manifest as thin, stratified materials with a more scattered configuration. The MoS<sub>2</sub> nanosheets appear as flexible, overlapping layers, offering an extensive surface area for interaction with Cu-MOF. The Cu-MOF/MoS<sub>2</sub> composite preserves the structural integrity of both constituents, with MoS<sub>2</sub> nanosheets uniformly distributed inside the porous framework of the Cu-MOF. This combination increases the composite's surface area and yields a highly organized material appropriate for diverse catalytic and adsorption applications.

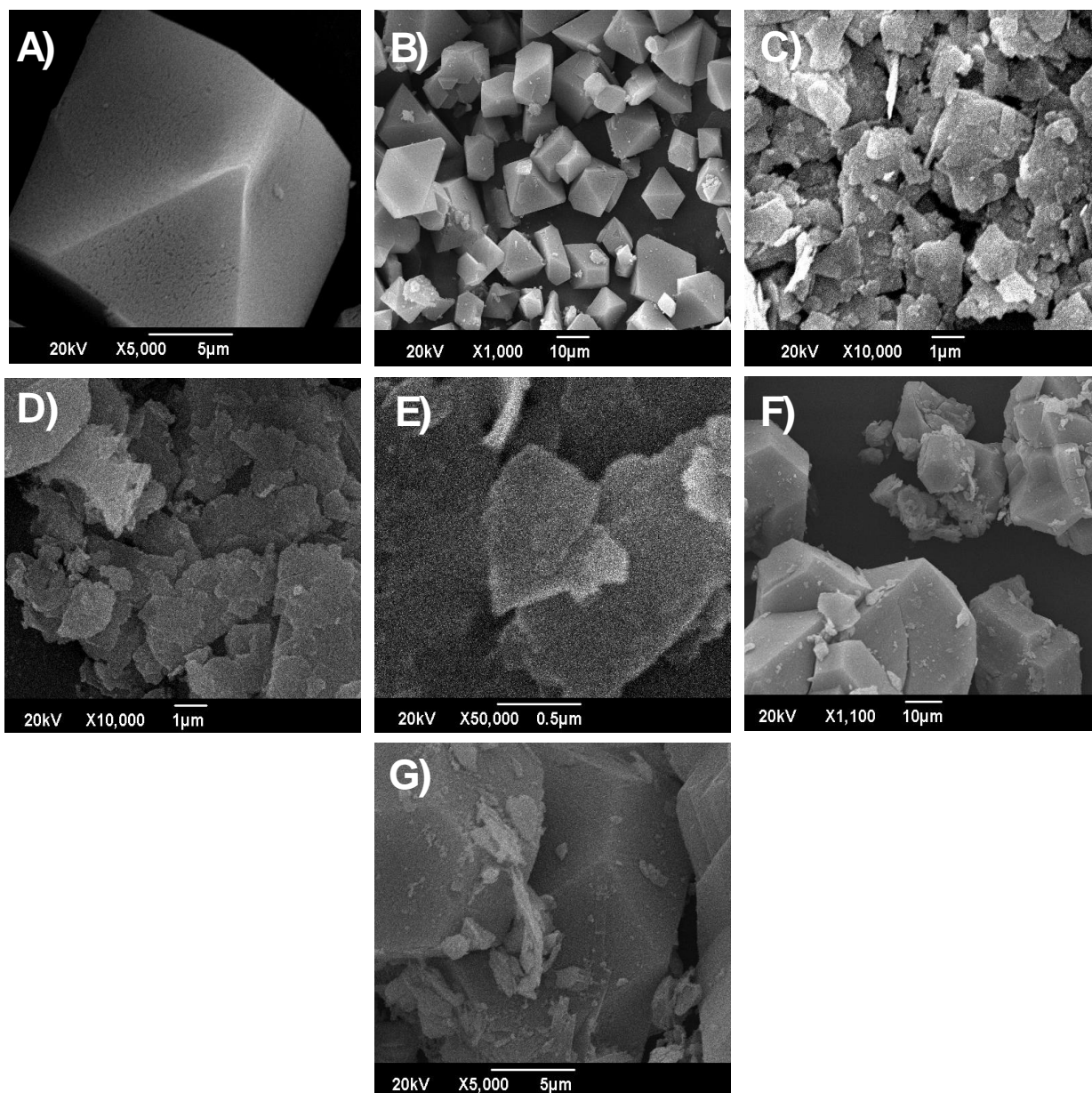


**Figure 5.1:** SEM Results of investigated Cu-MOF (A,B), Bulk MoS<sub>2</sub> (C), MoS<sub>2</sub> (D,E) and Cu-MOF/MoS<sub>2</sub> Nanocomposite (F,G).

## 5.2 X-ray diffraction Analysis

X-ray diffraction (XRD) was performed to examine the structural composition of the fabricated samples. The diffracted intensities were quantified within the range of 10° to 80°. Figure 5.2 illustrates the morphological features of Bulk MoS<sub>2</sub>, Cu-MOF, MoS<sub>2</sub>, and the Cu-MOF/MoS<sub>2</sub> nanocomposite.

The XRD pattern of the Cu MOF displayed prominent peaks at  $2\theta$  values of 5.82°, 6.72°, 9.51°, 11.15°, 11.66°, and 13.46°, corresponding to the crystal planes (111), (200), (220), (311), (222),

and (400). The observed peaks corresponded with the crystal planes documented in the literature (JCPDS No. 00-065-1028). The distinctly defined sharp peaks indicate a high level of crystallinity in the structure and a considerable particle size [109].

The XRD pattern of bulk MoS<sub>2</sub> had prominent peaks at 2θ values of 14.37°, 32.67°, 33.50°, 35.87°, 39.53°, 44.15°, and 49.78°, corresponding to the crystal planes (002), (100), (101), (102), (103), (006), and (105). In comparison to bulk MoS<sub>2</sub>, the XRD pattern of MoS<sub>2</sub> nanosheets exhibited unique peaks at 2θ values of 14.37°, 39.53°, 44.15°, and 49.78°, which correspond to the crystal planes (002), (103), (006), and (105), respectively. The observed peaks corresponded with the documented crystal planes in the literature (JCPDS No. 00-037-1492). The MoS<sub>2</sub> nanosheets had a crystalline, single-phase structure characterized by a hexagonal crystal system, with no impurities identified. The expansion of the (002) the number of stacked layers within the nanosheets, hence validating successful layer reduction [110].

The XRD data of the 9% Cu-MOF/MoS<sub>2</sub> nanocomposite predominantly corresponds with that of pure Cu-MOF, attributable to its greater proportion in the composite. The pronounced and prominent peaks in the XRD pattern validate that Cu-MOF is highly crystalline and maintains its crystalline structure throughout the synthesis of the composite, as observed in pure Cu-MOF. Furthermore, minor intensity peaks are seen at 14.45°, 41.06°, and 51.91°, aligning with the (003), (015), and (018) planes, respectively. The planes are indexed to MoS<sub>2</sub> nanosheets, so proving the presence of MoS<sub>2</sub> in the nanocomposite.

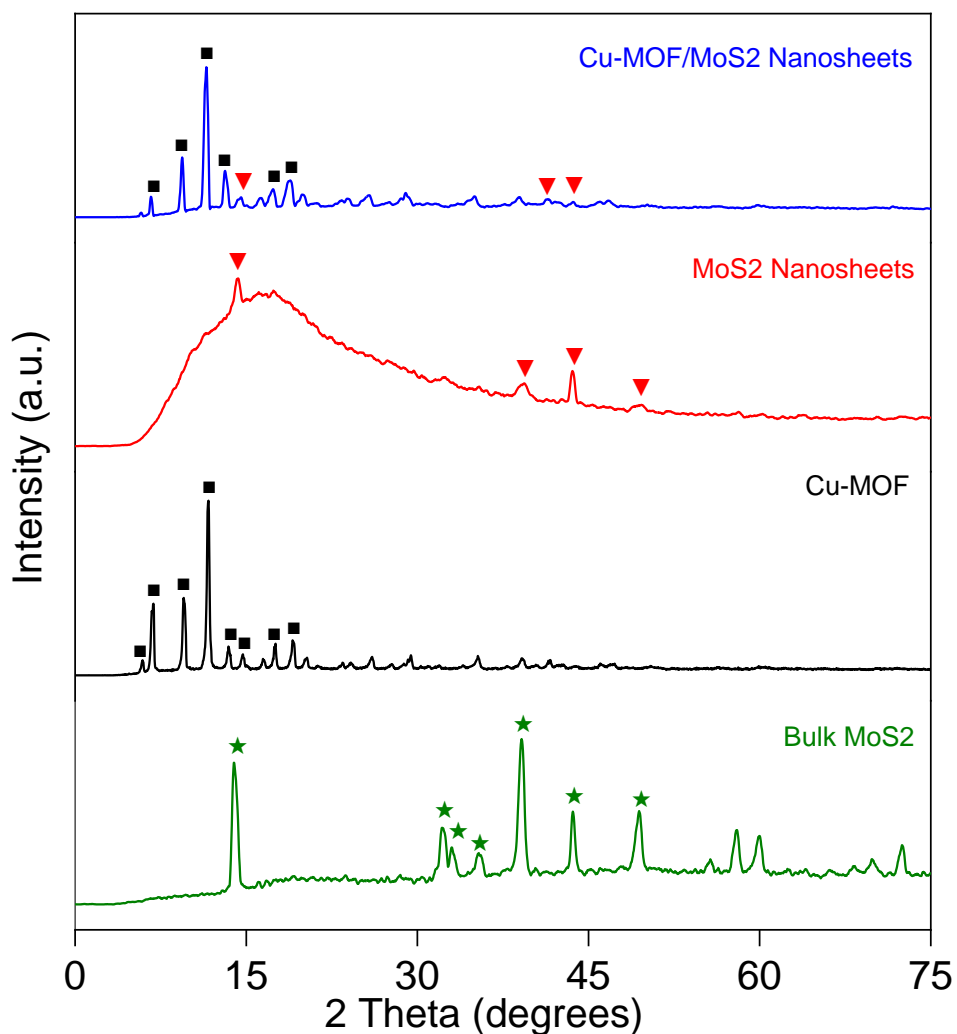


**Figure 5.1:** XRD Results of investigated Cu-MOF, MoS<sub>2</sub> and Cu-MOF/MoS<sub>2</sub> Nanocomposite.

### 5.3 Fourier Transform Infra-Red Spectroscopy

The FTIR spectra of all manufactured samples were compared within the wavenumber range of 4000 to 500  $\text{cm}^{-1}$ , as illustrated in Figure 5.3. The spectra of Cu MOF display a notable vibration at 724  $\text{cm}^{-1}$ , ascribed to the stretching of Cu-O bonds. This indicates that oxygen atoms are interacting with copper ions. The band observed at a wavenumber of 1425  $\text{cm}^{-1}$  is attributed to the vibrations of C-C bonds in the aromatic ring. The peak at 1357  $\text{cm}^{-1}$  corresponds to the stretching of C-O bonds in carboxylic acid functional groups. The

asymmetric stretching vibrations of the carboxylate groups generate the 1636  $\text{cm}^{-1}$  vibrational band in the MOF linker. Nonetheless, this band may also emerge via the elongation of the benzene ring and the vibrational distortion of water molecules. A large signal between 3100 and 3600  $\text{cm}^{-1}$  indicates the presence of water molecules that are loosely associated with the Cu MOF complex. This peak results from the stretching vibrations of hydroxyl groups in water molecules [109, 111].

A significant peak at approximately 470  $\text{cm}^{-1}$  is indicative of Mo-S stretching vibrations, hence affirming the existence of  $\text{MoS}_2$ . The broad bands in the 3300-3500  $\text{cm}^{-1}$  range signify O-H stretching vibrations, presumably from adsorbed moisture, whilst the faint peaks near 1600  $\text{cm}^{-1}$  imply the existence of adsorbed water molecules. The spectrum characteristics validate the effective exfoliation of  $\text{MoS}_2$  nanosheets and the existence of surface-adsorbed species [112].

The FTIR spectrum of the Cu-MOF/ $\text{MoS}_2$  nanocomposite displays unique peaks corresponding to each component of the composite. The distinctive peaks of Cu-MOF are clear, including the C=O stretching vibration at around 1650  $\text{cm}^{-1}$  and the C-H stretching in the range of 2900-3000  $\text{cm}^{-1}$ , thereby affirming the integrity of the MOF's organic framework. The existence of  $\text{MoS}_2$  is signified by Mo-S stretching vibrations near 470  $\text{cm}^{-1}$ . The unique peaks indicate the effective incorporation of Cu-MOF and  $\text{MoS}_2$  in the nanocomposite, affirming the structural integrity of both constituents inside the composite.

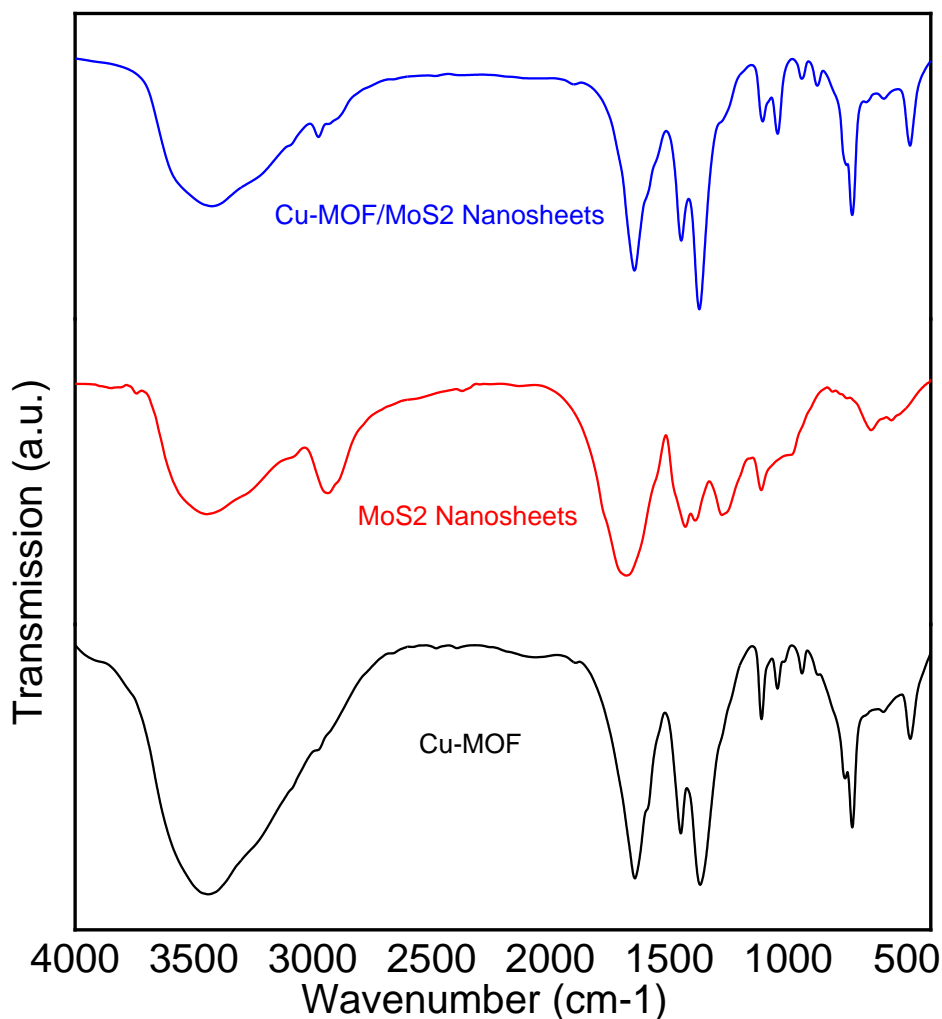


**Figure 5.2:** FTIR Results of investigated Cu-MOF, MoS<sub>2</sub> and Cu-MOF/MoS<sub>2</sub> Nanocomposite.

#### 5.4 AFM

Atomic Force Microscopy analysis indicated a thickness of around 170 nm for the MoS<sub>2</sub> bulk specimen. The considerable thickness signifies the presence of numerous layers in the bulk material, featuring step edges and layered structures typical of its crystalline form. The thickness of the MoS<sub>2</sub> nanosheets was measured at 7 nm, indicating a few layers of MoS<sub>2</sub>, with each monolayer typically measuring 1 nm. The significant decrease in thickness underscores the effective exfoliation process, yielding thin, stacked nanosheets ideal for applications requiring a high surface area-to-volume ratio.

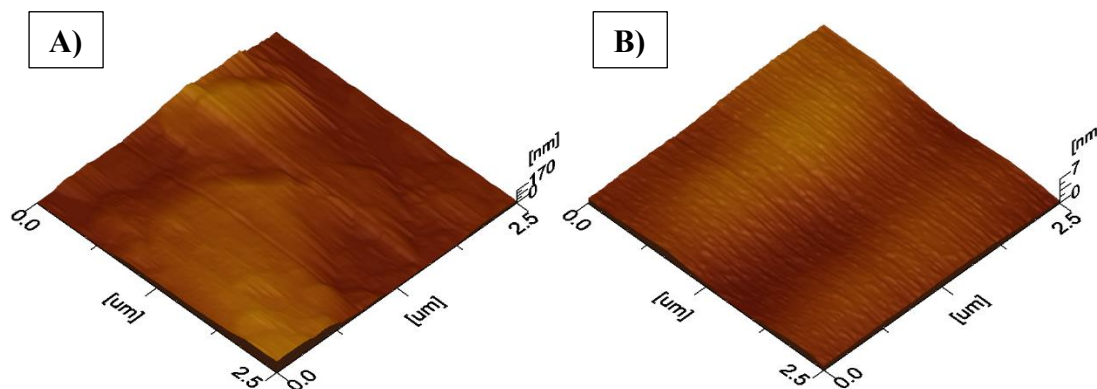


**Figure 5.4:** AFM of Bulk MoS<sub>2</sub> and MoS<sub>2</sub> Nanosheets

## 5.5 Adsorption Study

### 5.5.1 Stock Solution

For analyzing adsorption isotherm and kinetic models, a 1000 ppm concentrated MB solution was prepared. The following formula was used to dilute this solution until it reached a concentration of 25 ppm:

$$C_1V_1 = C_2V_2$$

A 25 ppm solution was diluted to make solutions with concentrations of 0, 5, 10, 15, and 20 ppm. These solutions were then used to create a calibration curve. The concentration of the dye was determined using a linear relationship.

### 5.5.2 Experimentation

Adsorption experiments were performed by varying the factors that can affect the adsorption process of MB. Following effects have been studied for each adsorbent.

- Contact time
- Adsorbent variation
- Adsorbate variation

The test involved the addition of 0.075 gram of adsorbent material to a 50 ml container of MB (25 ppm) with continuous stirring at 400 rpm. After a duration of 5 minutes to 240 minutes, a volume of 5 ml of eliquate was extracted from the mixture, and the adsorbent material was isolated using centrifugation at a speed of 4000 revolutions per minute. The mixture underwent

centrifugation for a duration of 10 minutes to separate the nanocomposite. The concentration of dye in the solution was determined using a UV-Vis spectrophotometer at the maximum absorbance wavelength ( $\lambda_{max}$ ) of MB, which is 665 nm. To maintain the desired pH value for the pH study, NaOH and HCl solutions with concentrations of 1.0 M were added. The effects of absorbent and adsorbate were also analyzed by changing their concentrations and keeping all other parameters unchanged.

Adsorption efficiency was determined by using the formula:

$$\text{Adsorption Efficiency (R\%)}: \frac{(\text{Initial conc.} - \text{Final conc.})}{\text{Final conc.}} \times 100$$

### 5.5.3 Effect of Contact time on Adsorption

The effect of time for adsorption was studied from 5 to 360 mins for each adsorbent, where temperature was 25°C and pH was 5 (constant parameters). For all adsorbents adsorption increases with increasing time until equilibrium time has reached. After equilibrium time no further adsorption was observed because surface coverage of each adsorbent reaches to its maximum. After reaching the saturation point adsorption becomes constant. Contact time for each adsorbent is given in table 5.1. Table 5.1: % Absorbance of Cu-MOF, MoS<sub>2</sub> and Cu-MOF/MoS<sub>2</sub> Nanocomposite with respect to Time

**Table 5.1:** % Absorbance of Cu-MOF, MoS<sub>2</sub> and Cu-MOF/MoS<sub>2</sub> Nanocomposite with respect to Time

Contact time	% Absorbance		
	Cu-MOF	MoS <sub>2</sub>	Cu-MOF@ MoS <sub>2</sub>
0 min	1.4701	1.4704	1.9845
10 min	8.5758	7.8560	8.7095
30 min	19.794	7.9280	33.7641
60 min	34.7558	11.7532	55.1384
120 min	51.9280	16.0308	60.3897
180 min	56.6478	21.5629	70.2527
240 min	59.7635	24.1336	78.0154
300 min	59.8476	24.8946	79.8868
360 min	59.8663	25.0077	79.9280



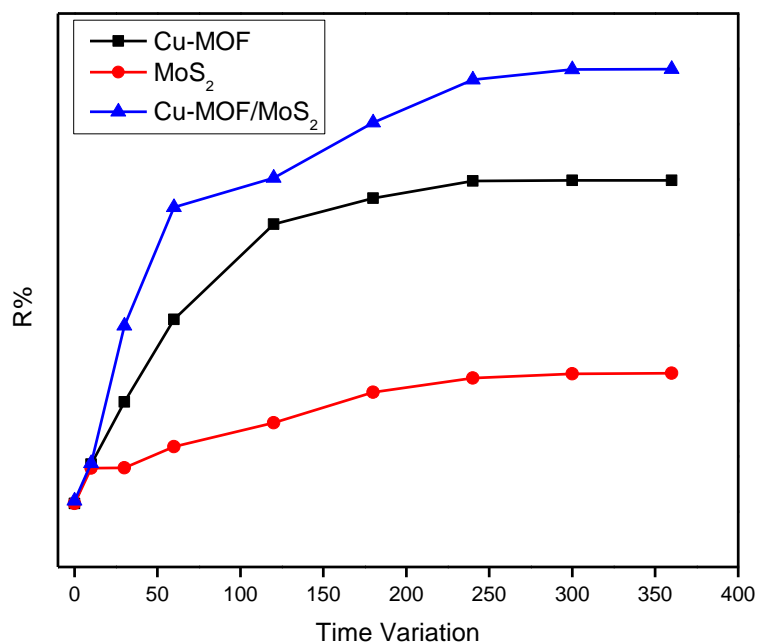


**Figure 5.4:** Trend of removal efficiency of Cu-MOF, MoS<sub>2</sub> and Cu-MOF/MoS<sub>2</sub> Nanocomposite with respect to Time.

#### 5.5.4 Effect of adsorbent dosage on adsorption of MB

The optimum adsorbent dosage for Cu-MOF, MoS<sub>2</sub> and its composite was determined by performing adsorption experiments at various initial concentrations keeping all other parameters constant. As the adsorbent dosage increases adsorption process increases and reaches to its maximum but as the adsorbent dosage increases after a certain level adsorption decreases. Lower adsorption at higher conditions is due to decrease in active sites because of particle aggregations.

**Table 5.2:** % Absorbance of Cu-MOF, MoS<sub>2</sub> and Cu-MOF/MoS<sub>2</sub> Nanocomposite with respect to adsorbent dosage.

Adsorbent Dose	% Absorbance		
	Cu-MOF	MoS <sub>2</sub>	Cu-MOF@ MoS <sub>2</sub>
6.25 mg	3.3213	3.3213	10.8380
12.5 mg	16.8637	5.3161	24.4832
25 mg	32.6580	13.5321	51.3110
50 mg	51.9280	16.0308	60.2673
75 mg	65.6966	16.6683	75.5372

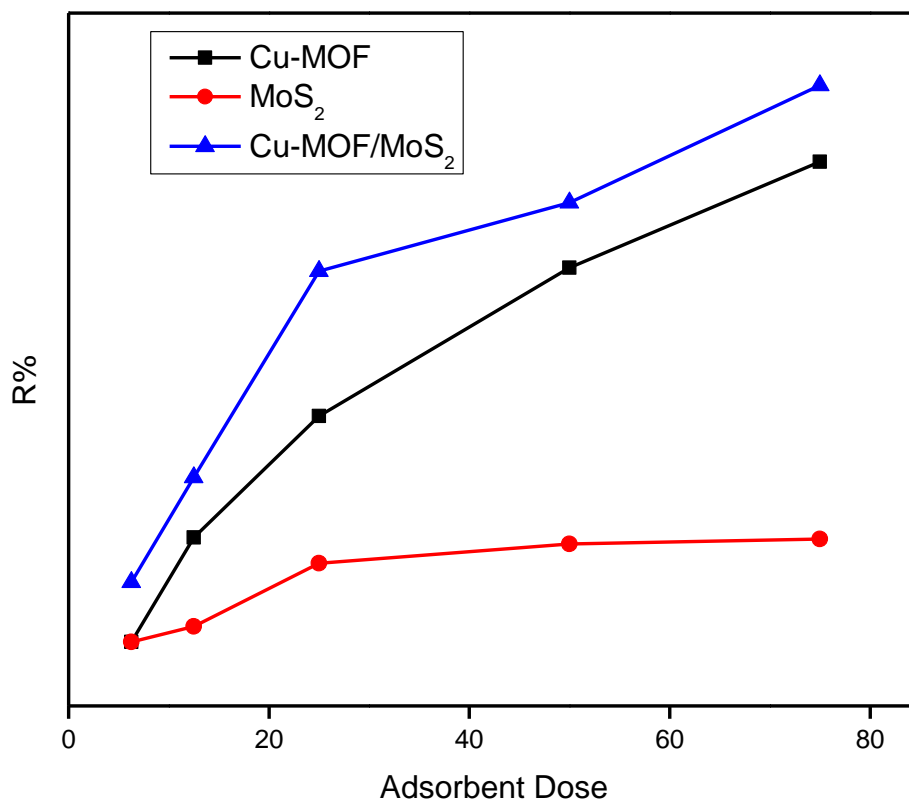


**Figure 5.5:** Trend of removal efficiency of Cu-MOF, MoS<sub>2</sub> and Cu-MOF/MoS<sub>2</sub> Nanocomposite with respect to adsorbent dosage.

### 5.5.5 Effect of initial concentration of MB on adsorption

MB uptake of Cu-MOF, MoS<sub>2</sub> and its composites increase with increase in chromium concentration. When all the adsorption sites are occupied, the adsorption process ends. No further increase in removal efficiency is observed. By increasing the chromium concentration removal efficiency increases but after reaching the optimum concentration adsorption process becomes constant because the active sites are occupied.

**Table 5.3:** % Absorbance of Cu-MOF, MoS<sub>2</sub> and Cu-MOF/MoS<sub>2</sub> Nanocomposite with respect to Initial concentration of MB.

Adsorbate Variation	% Absorbance		
	Cu-MOF	MoS <sub>2</sub>	Cu-MOF@ MoS <sub>2</sub>
5 ppm	81.1002	92.4215	92.6066
10 ppm	72.2673	67.3830	92.2159
15 ppm	66.2622	62.5501	77.4704
25 ppm	39.4241	16.0308	60.2673

50 ppm	13.3367	12.2673	52.6272
100 ppm	0.4832	3.3213	41.0385

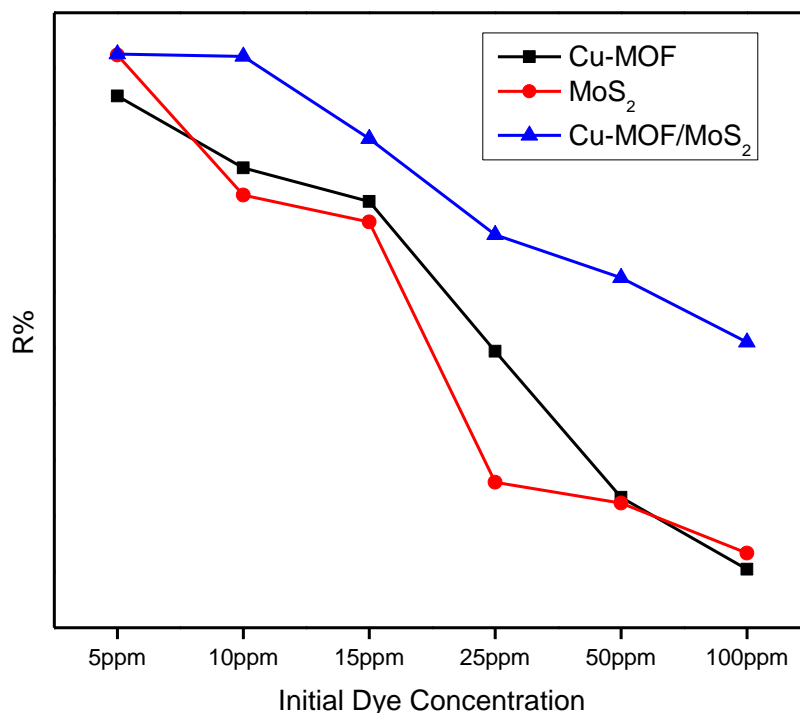


**Figure 5.5:** Trend of removal efficiency of Cu-MOF, MoS<sub>2</sub> and Cu-MOF/MoS<sub>2</sub> Nanocomposite with respect to Initial concentration of MB.

## 5.6 Adsorption Kinetics

The adsorption kinetics of MB onto Cu-MOF, MoS<sub>2</sub>, and Cu-MOF/MoS<sub>2</sub> nanocomposite were examined by non-linear fitting of both the pseudo-first order and pseudo-second order models. The experimental results were analyzed using these models to ascertain the rate constants ( $k_1$ ,  $k_2$ ) and the equilibrium adsorption capacity ( $Q_e$ ). An analysis of the  $R^2$  values for both models elucidate the appropriateness of each kinetic model in characterizing the adsorption process.

### 5.6.1 Pseudo-first order Model

Table 5.4 displays the  $R^2$  values for Cu-MOF, MoS<sub>2</sub>, and Cu-MOF/MoS<sub>2</sub> Nanocomposite in the pseudo-first-order model, which were 0.99, 0.93, and 0.98, respectively. The elevated  $R^2$  values, particularly for Cu-MOF (0.99) and the composite (0.98), suggest that the pseudo-first-order model accurately represents the experimental data. In the instance of MoS<sub>2</sub>, a  $R^2$  value of 0.93 indicates a marginally lesser degree of fit compared to Cu-MOF and the composite, albeit

remaining quite high. This may suggest that the adsorption mechanism for MoS<sub>2</sub> diverges marginally from the assumptions of the pseudo-first-order model, which generally characterizes physisorption occurring on exterior surfaces.

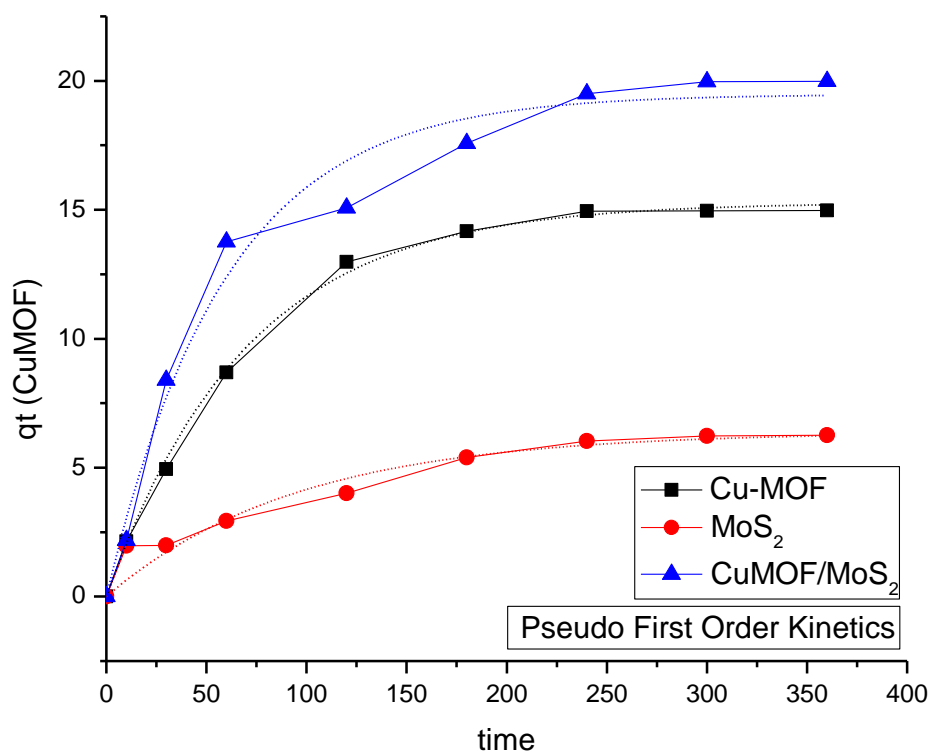


**Figure 5.6:** Pseudo first order for Cu-MOF, MoS<sub>2</sub> and Cu-MOF/MoS<sub>2</sub> Nanocomposite.

### 5.6.2 Pseudo-second order Model

The pseudo-second-order model, commonly utilized to depict chemisorption that involves electron sharing or exchange, was also employed. The R<sup>2</sup> values for this model were 0.98 for Cu-MOF, 0.95 for MoS<sub>2</sub>, and 0.98 for the composite (Table 5.4). The values demonstrate a robust connection between the experimental and computed data, with the pseudo-second-order model yielding a marginally superior fit for MoS<sub>2</sub> in comparison to the pseudo-first-order model. The fit for Cu-MOF and the composite was similarly high in both kinetic models, exhibiting R<sup>2</sup> values of 0.98.

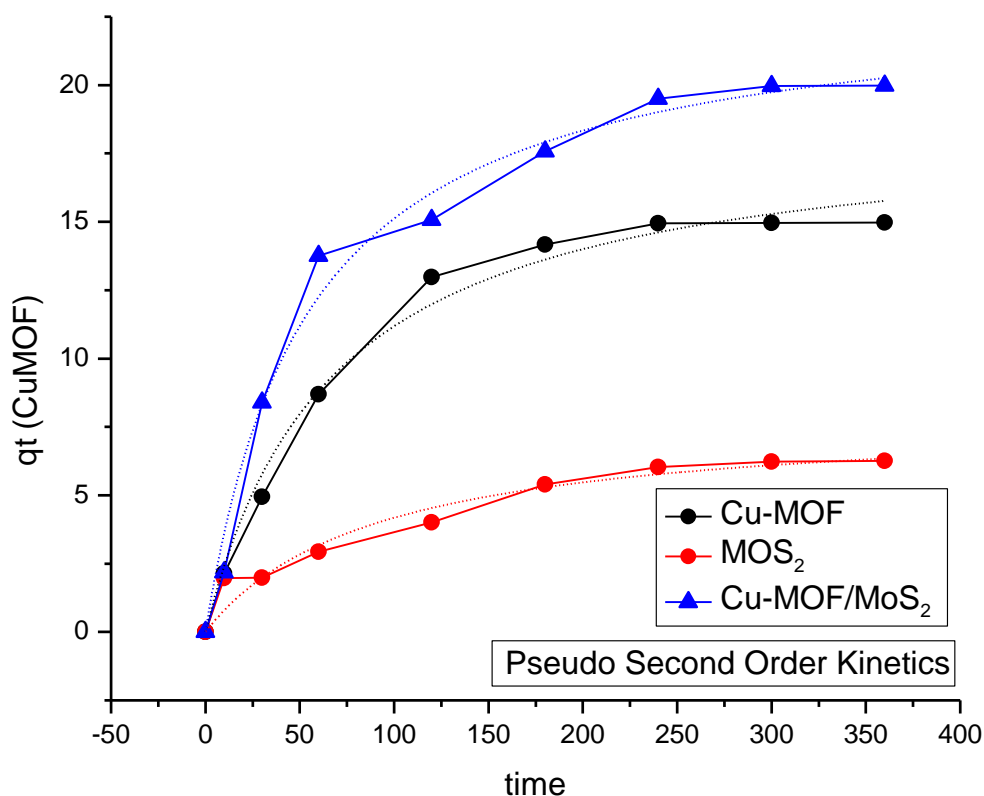


**Figure 5.7:** Pseudo second order for Cu-MOF, MoS<sub>2</sub> and Cu-MOF/MoS<sub>2</sub> Nanocomposite.

For Cu-MOF and the composite, both the pseudo-first order and pseudo-second-order models had nearly identical  $R^2$  values (0.99 and 0.98, respectively). This indicates that the adsorption process for these materials can be accurately characterized by any model. For MoS<sub>2</sub>, the pseudo-second-order model, with a  $R^2$  value of 0.95, demonstrates a somewhat superior match compared to the pseudo-first-order model ( $R^2 = 0.93$ ). This suggests that the adsorption of MB onto MoS<sub>2</sub> may entail a chemisorption process, characterized by a greater contact between the adsorbate and adsorbent than that of simple physisorption.

In summary, both models effectively characterize the adsorption kinetics for all adsorbents; however, the pseudo-first-order model exhibits marginally superior performance for Cu-MOF and the composite, while the pseudo-second-order model is more suitable for MoS<sub>2</sub>. The accuracy of fit, as evidenced by the  $R^2$  values, illustrates the capacity of both models to characterize the adsorption process, but the predominant mechanism may vary between materials.

**Table 5.4:** Non-linear analysis of kinetic adsorption parameters for MB dye removal by Cu-MOF, MoS<sub>2</sub> and Cu-MOF/MoS<sub>2</sub>

Dye	Adsorbent	PFO				PSO		
		Qe (mg g <sup>-1</sup> ) Experimental	Qe (mg g <sup>-1</sup> ) calculated	k1 (min <sup>-1</sup> )	R <sup>2</sup>	Qe (mg g <sup>-1</sup> ) calculated	k2 (min <sup>-1</sup> )	R <sup>2</sup>
MB	Cu-MOF	14.9	15.28	0.014	0.99	18.71	7.932x10 <sup>-4</sup>	0.98
	MoS <sub>2</sub>	6.2	6.38	0.01053	0.93	7.908	0.00141	0.92
	Cu-MOF/MoS <sub>2</sub>	19.9	19.47	0.016	0.98	23.30	7.928x10 <sup>-4</sup>	0.98

The elevated R<sup>2</sup> values for both the pseudo-first order and pseudo-second order models of Cu-MOF and the composite indicate a complex adsorption mechanism potentially including both physisorption and chemisorption. The findings for MoS<sub>2</sub> support the pseudo-second-order model, indicating that chemisorption is the predominant process. These findings offer significant insights into the interactions between MB and the adsorbents, which may inform further optimization for pollutant removal applications.

## 5.7 Adsorption Isotherm

The adsorption characteristics of MB on Cu-MOF, MoS<sub>2</sub>, and their composite were evaluated utilizing the Langmuir and Freundlich isotherm models. The efficacy of these models was evaluated via linear regression, and the R<sup>2</sup> values were contrasted to ascertain which model more accurately represents the adsorption process.

### 5.7.1 Langmuir Isotherm Model

The Langmuir model proposes monolayer adsorption over a uniform surface. The linear fitting results indicated R<sup>2</sup> values of 0.84 for Cu-MOF, 0.87 for MoS<sub>2</sub>, and 0.94 for Cu-MOF/MoS<sub>2</sub> Nanocomposite. The values indicate that the Langmuir model adequately matches the data for the Cu-MOF/MoS<sub>2</sub> Nanocomposite but is less effective for Cu-MOF and MoS<sub>2</sub>. The

diminished  $R^2$  values for Cu-MOF and MoS<sub>2</sub> suggest that the Langmuir model may inadequately represent their adsorption characteristics, maybe owing to surface heterogeneity or the occurrence of multilayer adsorption.

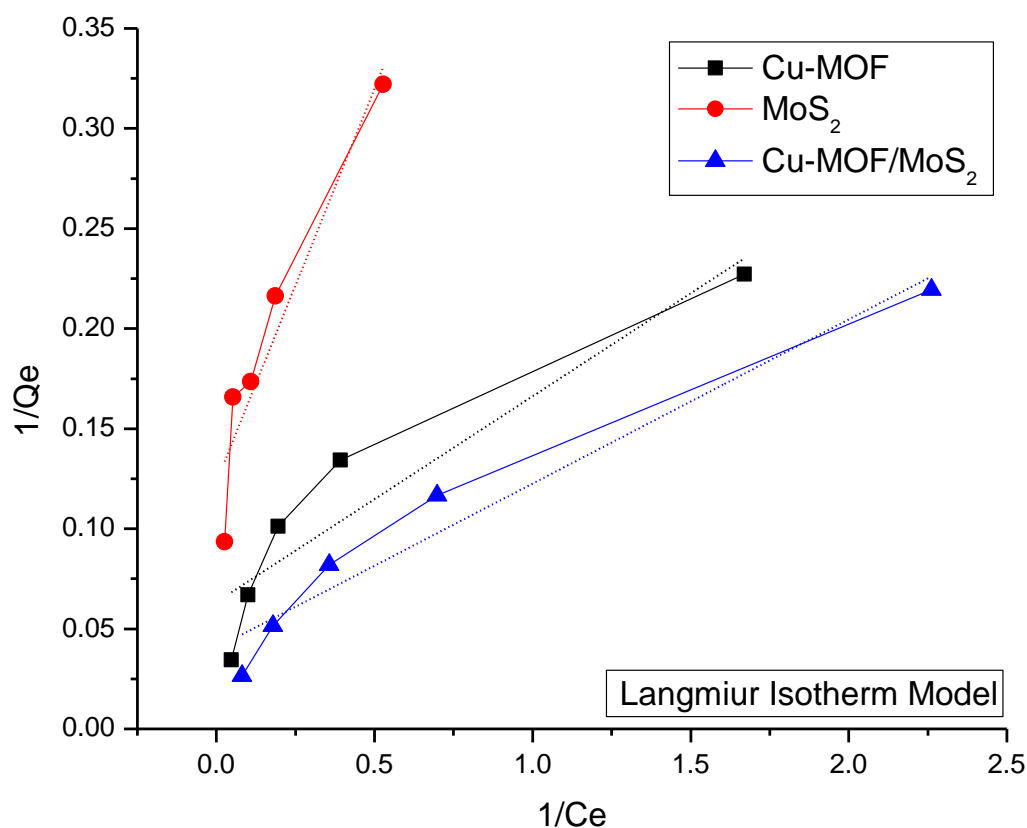


**Figure 5.8:** Langmuir Isotherm Model for Cu-MOF, MoS<sub>2</sub> and Cu-MOF/MoS<sub>2</sub> Nanocomposite.

### 5.7.2 Freundlich Isotherm Model

The Freundlich model, which proposes adsorption on a heterogeneous surface, gave  $R^2$  values of 0.93 for Cu-MOF, 0.91 for MoS<sub>2</sub>, and 0.98 for the Cu-MOF/MoS<sub>2</sub> Nanocomposite. The elevated  $R^2$  values, especially for the composite, indicate that the Freundlich model more accurately characterizes the adsorption process for all materials. The superior fit of Cu-MOF and MoS<sub>2</sub> relative to the Langmuir model suggests that these materials possess more intricate surface properties with heterogeneous adsorption site energies.

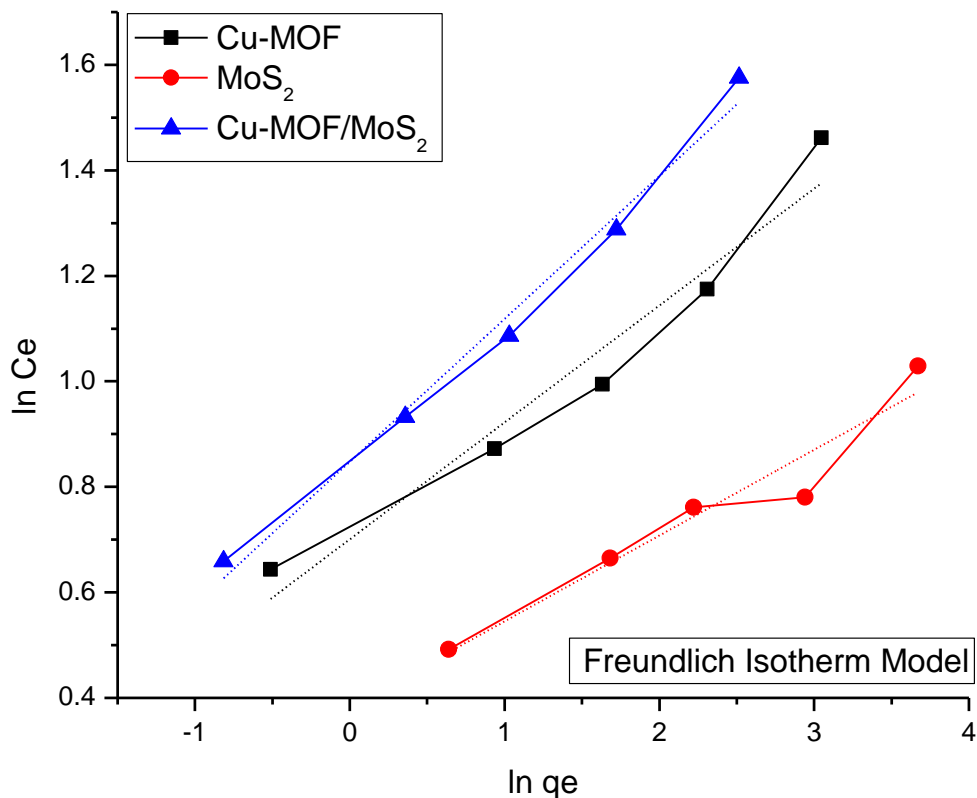


**Figure 5.9:** Freundlich Isotherm Model for Cu-MOF, MoS<sub>2</sub> and Cu-MOF/MoS<sub>2</sub> Nanocomposite

Upon comparison of the  $R^2$  values for both models, the Freundlich model consistently demonstrated superior fit across all adsorbents. The elevated  $R^2$  values for the Freundlich model, particularly for the composite, suggest that adsorption probably takes place on a heterogeneous surface characterized by a spectrum of adsorption site energies. The Langmuir model indicates monolayer adsorption; nevertheless, the lower  $R^2$  values for Cu-MOF and MoS<sub>2</sub> underscore the more intricate adsorption characteristics of these materials.

**Table 5.5:** Freundlich Isotherm Model for Cu-MOF, MoS<sub>2</sub> and Cu-MOF/MoS<sub>2</sub> Nanocomposite.

Dye	Adsorbent	Langmuir Isotherm constant			Freundlich Isotherm constant		
		$K_L$ (L/mg)	$Q_m$ (mg/g)	$R^2$	$K_f$ (mg/g)	$1/n$	$R^2$
MB							



	Cu-MOF	16.66	0.60	0.84	2.01	0.22152	0.93
	MoS <sub>2</sub>	8.33	0.30	0.87	1.46	0.16259	0.91
	Cu-MOF/MoS <sub>2</sub>	24.648	0.494	0.94	2.31	0.2708	0.98

The Freundlich model more accurately represents the adsorption data for Cu-MOF, MoS<sub>2</sub>, and the composite, indicating heterogeneous surface interactions. The Langmuir model, while effective for characterizing monolayer adsorption, is inadequate for these materials, particularly Cu-MOF and MoS<sub>2</sub>, which display a broader range of adsorption site energies.

## CHAPTER 6: CONCLUSIONS

This study effectively synthesized and evaluated a novel Cu-MOF/MoS<sub>2</sub> nanocomposite, revealing its efficacy as an adsorbent for eliminating Methylene Blue (MB) dye from aqueous solutions. Combining Cu-based metal-organic frameworks (Cu-MOF) and Molybdenum Disulfide (MoS<sub>2</sub>) demonstrated improved adsorption characteristics, with the nanocomposite outperforming its constituent elements.

The characterization results validated the effective incorporation of MoS<sub>2</sub> nanosheets into the Cu-MOF framework, resulting in improved surface area and structural integrity. The adsorption tests, comprising the influences of contact time, adsorbent dosage, and initial dye concentration, demonstrated that the Cu-MOF/MoS<sub>2</sub> nanocomposite exhibited a markedly superior adsorption capability compared to Cu-MOF or MoS<sub>2</sub> individually. The Freundlich isotherm model exhibited the optimal fit for the adsorption data, signifying that adsorption probably takes place on a heterogeneous surface characterized by a spectrum of adsorption site energies.

The kinetic experiments indicated that the adsorption process adhered to a pseudo-second-order model, suggesting that chemisorption was the predominant mechanism in dye removal.

The improved adsorption capacity and advantageous kinetics of the Cu-MOF/MoS<sub>2</sub> nanocomposite result from the synergistic interaction between the elevated surface area and porosity of Cu-MOF and the enhanced conductivity and reactivity of MoS<sub>2</sub> nanosheets. The results highlight the efficacy of Cu-MOF/MoS<sub>2</sub> as a reusable and economical adsorbent for wastewater treatment, especially in the elimination of toxic dyes such as Methylene Blue.

### **FUTURE RECOMMENDATIONS:**

Future studies ought to concentrate on producing the Cu-MOF/MoS<sub>2</sub> nanocomposite at a larger scale, investigating how it would be able to eliminate additional organic contaminants from wastewater, and maximizing its regeneration and reusability in workplaces. Moreover, additional investigation into other metal-organic frameworks and two-dimensional materials may yield enhanced adsorbent performance.

## REFERENCES

- [1] P. H. Gleick and M. Palaniappan, "Peak water limits to freshwater withdrawal and use," *Proceedings of the National Academy of Sciences*, vol. 107, no. 25, pp. 11155-11162, 2010.
- [2] L. Liao, E. Kovalska, J. Regner, Q. Song, and Z. Sofer, "Two-Dimensional Van Der Waals Thin Film and Device," *Small*, vol. 20, no. 4, p. 2303638, 2024.
- [3] K. Hunger, *Industrial dyes: chemistry, properties, applications*. John Wiley & Sons, 2007.
- [4] M. Tkalec, A. Sutlovic, and M. I. Glogar, "Ecological, Economic and Social Aspects of Textile Dyes," *Economic and Social Development: Book of Proceedings*, pp. 69-79, 2022.
- [5] J. Sharma, S. Sharma, and V. Soni, "Classification and impact of synthetic textile dyes on Aquatic Flora: A review," *Regional Studies in Marine Science*, vol. 45, p. 101802, 2021.
- [6] M. Shabir *et al.*, "A review on recent advances in the treatment of dye-polluted wastewater," *Journal of Industrial and Engineering Chemistry*, vol. 112, pp. 1-19, 2022.
- [7] L. A. Mokif, "Removal methods of synthetic dyes from industrial wastewater: a review," *Mesopotamia Environmental Journal (mesop. environ. j) ISSN: 2410-2598*, vol. 5, no. 1, pp. 23-40, 2019.
- [8] M. T. Yagub, T. K. Sen, S. Afroze, and H. M. Ang, "Dye and its removal from aqueous solution by adsorption: a review," *Advances in colloid and interface science*, vol. 209, pp. 172-184, 2014.
- [9] S. De Gisi, G. Lofrano, M. Grassi, and M. Notarnicola, "Characteristics and adsorption capacities of low-cost sorbents for wastewater treatment: A review," *Sustainable Materials and Technologies*, vol. 9, pp. 10-40, 2016.
- [10] F. W. John Thomas and B. Crittenden, *Adsorption technology and design*. Butterworth-Heinemann, 1998.
- [11] H. Zollinger, *Color chemistry: syntheses, properties, and applications of organic dyes and pigments*. John Wiley & Sons, 2003.
- [12] M. Islam and M. Mostafa, "Textile dyeing effluents and environment concerns—a review," *J Environ Sci Nat Resour*, vol. 11, no. 1, pp. 131-144, 2018.

- [13] J. G. Marks Jr, B. E. Anderson, and V. A. DeLeo, *Contact & occupational dermatology*. JP Medical Ltd, 2016.
- [14] G. M. Tiboni and D. Lamonaca, "Transplacental exposure to methylene blue initiates teratogenesis in the mouse: preliminary evidence for a mechanistic implication of cyclic GMP pathway disruption," *Teratology*, vol. 64, no. 4, pp. 213-220, 2001.
- [15] R. Liversidge, G. Lloyd, D. Wase, and C. Forster, "Removal of Basic Blue 41 dye from aqueous solution by linseed cake," *Process Biochemistry*, vol. 32, no. 6, pp. 473-477, 1997.
- [16] C. Lin *et al.*, "Carbon dots embedded metal organic framework@ chitosan core-shell nanoparticles for vitro dual mode imaging and pH-responsive drug delivery," *Microporous and Mesoporous Materials*, vol. 293, p. 109775, 2020.
- [17] K. Asha, R. Bhattacharjee, and S. Mandal, "Complete transmetalation in a metal-organic framework by metal ion metathesis in a single crystal for selective sensing of phosphate ions in aqueous media," *Angewandte Chemie International Edition*, vol. 55, no. 38, pp. 11528-11532, 2016.
- [18] J. A. Mason *et al.*, "Methane storage in flexible metal-organic frameworks with intrinsic thermal management," *Nature*, vol. 527, no. 7578, pp. 357-361, 2015.
- [19] S. Zheng *et al.*, "Transition-metal (Fe, Co, Ni) based metal-organic frameworks for electrochemical energy storage," *Advanced Energy Materials*, vol. 7, no. 18, p. 1602733, 2017.
- [20] J. D. Sosa, T. F. Bennett, K. J. Nelms, B. M. Liu, R. C. Tovar, and Y. Liu, "Metal-organic framework hybrid materials and their applications," *Crystals*, vol. 8, no. 8, p. 325, 2018.
- [21] H. Furukawa, K. E. Cordova, M. O'Keeffe, and O. M. Yaghi, "The chemistry and applications of metal-organic frameworks," *Science*, vol. 341, no. 6149, p. 1230444, 2013.
- [22] S. Wuttke, M. Lismont, A. Escudero, B. Rungtaweevoranit, and W. J. Parak, "Positioning metal-organic framework nanoparticles within the context of drug delivery—a comparison with mesoporous silica nanoparticles and dendrimers," *Biomaterials*, vol. 123, pp. 172-183, 2017.
- [23] M. Zhao, C. Casiraghi, and K. Parvez, "Electrochemical exfoliation of 2D materials beyond graphene," *Chemical Society Reviews*, 2024.

- [24] K. B. Ibrahim, T. A. Shifa, S. Zorzi, M. G. Sendeku, E. Moretti, and A. Vomiero, "Emerging 2D materials beyond mxenes and TMDs: Transition metal carbodichalcogenides," *Progress in Materials Science*, p. 101287, 2024.
- [25] T. Nawz, A. Safdar, M. Hussain, D. Sung Lee, and M. Siyar, "Graphene to Advanced MoS<sub>2</sub>: A Review of Structure, Synthesis, and Optoelectronic Device Application," *Crystals*, vol. 10, no. 10, p. 902, 2020.
- [26] K. S. Novoselov, L. Colombo, P. Gellert, M. Schwab, and K. Kim, "A roadmap for graphene," *nature*, vol. 490, no. 7419, pp. 192-200, 2012.
- [27] A. V. Kolobov, J. Tominaga, A. V. Kolobov, and J. Tominaga, "Emerging applications of 2D TMDCs," *Two-Dimensional Transition-Metal Dichalcogenides*, pp. 473-512, 2016.
- [28] Z. Xu, "Fundamental properties of graphene," in *Graphene*: Elsevier, 2018, pp. 73-102.
- [29] Y. Zhu *et al.*, "Graphene and graphene oxide: synthesis, properties, and applications," *Advanced materials*, vol. 22, no. 35, pp. 3906-3924, 2010.
- [30] H. Kim *et al.*, "Electrical, optical, and structural properties of indium–tin–oxide thin films for organic light-emitting devices," *Journal of applied physics*, vol. 86, no. 11, pp. 6451-6461, 1999.
- [31] Z. Zhen and H. Zhu, "Structure and properties of graphene," in *Graphene*: Elsevier, 2018, pp. 1-12.
- [32] K. Zhang, Y. Feng, F. Wang, Z. Yang, and J. Wang, "Two dimensional hexagonal boron nitride (2D-hBN): synthesis, properties and applications," *Journal of Materials Chemistry C*, vol. 5, no. 46, pp. 11992-12022, 2017.
- [33] A. Carvalho, M. Wang, X. Zhu, A. S. Rodin, H. Su, and A. H. Castro Neto, "Phosphorene: from theory to applications," *Nature Reviews Materials*, vol. 1, no. 11, pp. 1-16, 2016.
- [34] A. Favron *et al.*, "Exfoliating pristine black phosphorus down to the monolayer: photo-oxidation and electronic confinement effects," *arXiv preprint arXiv:1408.0345*, 2014.
- [35] J. Miao, L. Zhang, and C. Wang, "Black phosphorus electronic and optoelectronic devices," *2D Materials*, vol. 6, no. 3, p. 032003, 2019.
- [36] M. Naguib, V. N. Mochalin, M. W. Barsoum, and Y. Gogotsi, "25th anniversary article: MXenes: a new family of two-dimensional materials," *Advanced materials*, vol. 26, no. 7, pp. 992-1005, 2014.

- [37] K. Hantanasirisakul *et al.*, "Effects of synthesis and processing on optoelectronic properties of titanium carbonitride MXene," *Chemistry of Materials*, vol. 31, no. 8, pp. 2941-2951, 2019.
- [38] N. Podberezskaya, S. Magarill, N. Pervukhina, and S. Borisov, "Crystal chemistry of dichalcogenides MX<sub>2</sub>," *Journal of Structural Chemistry*, vol. 42, pp. 654-681, 2001.
- [39] X. Li and H. Zhu, "Two-dimensional MoS<sub>2</sub>: Properties, preparation, and applications," *Journal of Materiomics*, vol. 1, no. 1, pp. 33-44, 2015.
- [40] K. F. Mak, C. Lee, J. Hone, J. Shan, and T. F. Heinz, "Atomically thin MoS<sub>2</sub>: a new direct-gap semiconductor," *Physical review letters*, vol. 105, no. 13, p. 136805, 2010.
- [41] H. Zhang, "Ultrathin two-dimensional nanomaterials," *ACS nano*, vol. 9, no. 10, pp. 9451-9469, 2015.
- [42] D. Akinwande, N. Petrone, and J. Hone, "Two-dimensional flexible nanoelectronics," *Nature communications*, vol. 5, no. 1, p. 5678, 2014.
- [43] J. Gusakova *et al.*, "Electronic properties of bulk and monolayer TMDs: theoretical study within DFT framework (GVJ-2e method)," *physica status solidi (a)*, vol. 214, no. 12, p. 1700218, 2017.
- [44] N. Ortiz and S. E. Skrabalak, "On the dual roles of ligands in the synthesis of colloidal metal nanostructures," *Langmuir*, vol. 30, no. 23, pp. 6649-6659, 2014.
- [45] S. E. Skrabalak, B. J. Wiley, M. Kim, E. V. Formo, and Y. Xia, "On the polyol synthesis of silver nanostructures: glycolaldehyde as a reducing agent," *Nano letters*, vol. 8, no. 7, pp. 2077-2081, 2008.
- [46] S. Yang, P. Qiu, and G. Yang, "Graphene induced formation of single crystal Pt nanosheets through 2-dimensional aggregation and sintering of nanoparticles in molten salt medium," *Carbon*, vol. 77, pp. 1123-1131, 2014.
- [47] C. Tan *et al.*, "Recent advances in ultrathin two-dimensional nanomaterials," *Chemical reviews*, vol. 117, no. 9, pp. 6225-6331, 2017.
- [48] X. Cai, Y. Luo, B. Liu, and H.-M. Cheng, "Preparation of 2D material dispersions and their applications," *Chemical Society Reviews*, vol. 47, no. 16, pp. 6224-6266, 2018.
- [49] K. S. Novoselov *et al.*, "Electric field effect in atomically thin carbon films," *science*, vol. 306, no. 5696, pp. 666-669, 2004.

- [50] M. Zeng, Y. Xiao, J. Liu, K. Yang, and L. Fu, "Exploring two-dimensional materials toward the next-generation circuits: from monomer design to assembly control," *Chemical reviews*, vol. 118, no. 13, pp. 6236-6296, 2018.
- [51] H. Samassekou *et al.*, "Corrigendum: Viable route towards large-area 2D MoS<sub>2</sub> using magnetron sputtering (2017 2D Mater. 4 021002)," *2D Mater.*, vol. 4, no. 2, p. 021002, 2017.
- [52] R. Raccichini, A. Varzi, S. Passerini, and B. Scrosati, "The role of graphene for electrochemical energy storage," *Nature materials*, vol. 14, no. 3, pp. 271-279, 2015.
- [53] N. Sharma, P. Kumar, and M. K. Khanna, "Molybdenum Disulfide: A 2D Material," in *Emerging Applications of Novel Nanoparticles*: Springer, 2024, pp. 145-173.
- [54] H. Li, J. Wu, Z. Yin, and H. Zhang, "Preparation and applications of mechanically exfoliated single-layer and multilayer MoS<sub>2</sub> and WSe<sub>2</sub> nanosheets," *Accounts of chemical research*, vol. 47, no. 4, pp. 1067-1075, 2014.
- [55] V. P. Kumar and D. K. Panda, "Next generation 2D material molybdenum disulfide (MoS<sub>2</sub>): properties, applications and challenges," *ECS Journal of Solid State Science and Technology*, vol. 11, no. 3, p. 033012, 2022.
- [56] I. Shlyakhov *et al.*, "Measurement of direct and indirect bandgaps in synthetic ultrathin MoS<sub>2</sub> and WS<sub>2</sub> films from photoconductivity spectra," *Journal of Applied Physics*, vol. 129, no. 15, 2021.
- [57] X. Tong, E. Ashalley, F. Lin, H. Li, and Z. M. Wang, "Advances in MoS<sub>2</sub>-based field effect transistors (FETs)," *Nano-Micro Letters*, vol. 7, pp. 203-218, 2015.
- [58] M. A. R. Anjum, H. Y. Jeong, M. H. Lee, H. S. Shin, and J. S. Lee, "Efficient hydrogen evolution reaction catalysis in alkaline media by all-in-one MoS<sub>2</sub> with multifunctional active sites," *Advanced Materials*, vol. 30, no. 20, p. 1707105, 2018.
- [59] C. Cui *et al.*, "Three-dimensional carbon frameworks enabling MoS<sub>2</sub> as anode for dual ion batteries with superior sodium storage properties," *Energy Storage Materials*, vol. 15, pp. 22-30, 2018.
- [60] M. Ahmaruzzaman and V. Gadore, "MoS<sub>2</sub> based nanocomposites: An excellent material for energy and environmental applications," *Journal of Environmental Chemical Engineering*, vol. 9, no. 5, p. 105836, 2021.
- [61] M. R. Vazirisereshk, A. Martini, D. A. Strubbe, and M. Z. Baykara, "Solid lubrication with MoS<sub>2</sub>: a review," *Lubricants*, vol. 7, no. 7, p. 57, 2019.

- [62] S. Homaeigohar, "The nanosized dye adsorbents for water treatment," *Nanomaterials*, vol. 10, no. 2, p. 295, 2020.
- [63] K. Khan *et al.*, "Recent developments in emerging two-dimensional materials and their applications," *Journal of Materials Chemistry C*, vol. 8, no. 2, pp. 387-440, 2020.
- [64] Z. U. Zango *et al.*, "A critical review on metal-organic frameworks and their composites as advanced materials for adsorption and photocatalytic degradation of emerging organic pollutants from wastewater," *Polymers*, vol. 12, no. 11, p. 2648, 2020.
- [65] A. Haleem, A. Shafiq, S.-Q. Chen, and M. Nazar, "A comprehensive review on adsorption, photocatalytic and chemical degradation of dyes and nitro-compounds over different kinds of porous and composite materials," *Molecules*, vol. 28, no. 3, p. 1081, 2023.
- [66] S. Roy, J. Darabdhara, and M. Ahmaruzzaman, "Recent advances of Copper-BTC metal-organic frameworks for efficient degradation of organic dye-polluted wastewater: Synthesis, Mechanistic Insights and Future Outlook," *Journal of Hazardous Materials Letters*, p. 100094, 2023.
- [67] H. J. Song, S. You, X. H. Jia, and J. Yang, "MoS<sub>2</sub> nanosheets decorated with magnetic Fe<sub>3</sub>O<sub>4</sub> nanoparticles and their ultrafast adsorption for wastewater treatment," *Ceramics International*, vol. 41, no. 10, pp. 13896-13902, 2015.
- [68] X. Qiao, F. Hu, D. Hou, and D. Li, "PEG assisted hydrothermal synthesis of hierarchical MoS<sub>2</sub> microspheres with excellent adsorption behavior," *Materials Letters*, vol. 169, pp. 241-245, 2016.
- [69] V. Jabbari, J. Veleta, M. Zarei-Chaleshtori, J. Gardea-Torresdey, and D. Villagrán, "Green synthesis of magnetic MOF@ GO and MOF@ CNT hybrid nanocomposites with high adsorption capacity towards organic pollutants," *Chemical Engineering Journal*, vol. 304, pp. 774-783, 2016.
- [70] A. T. Massey, R. Gusain, S. Kumari, and O. P. Khatri, "Hierarchical microspheres of MoS<sub>2</sub> nanosheets: efficient and regenerative adsorbent for removal of water-soluble dyes," *Industrial & Engineering Chemistry Research*, vol. 55, no. 26, pp. 7124-7131, 2016.
- [71] H. Xie and X. Xiong, "A porous molybdenum disulfide and reduced graphene oxide nanocomposite (MoS<sub>2</sub>-rGO) with high adsorption capacity for fast and preferential adsorption towards Congo red," *Journal of environmental chemical engineering*, vol. 5, no. 1, pp. 1150-1158, 2017.



- [72] S. Han, K. Liu, L. Hu, F. Teng, P. Yu, and Y. Zhu, "Superior adsorption and regenerable dye adsorbent based on flower-like molybdenum disulfide nanostructure," *Scientific reports*, vol. 7, no. 1, p. 43599, 2017.
- [73] Z. Shi *et al.*, "Magnetic metal organic frameworks (MOFs) composite for removal of lead and malachite green in wastewater," *Colloids and Surfaces A: Physicochemical and Engineering Aspects*, vol. 539, pp. 382-390, 2018.
- [74] Y. Wu *et al.*, "Superior adsorption of methyl orange by h-MoS<sub>2</sub> microspheres: Isotherm, kinetics, and thermodynamic studies," *Dyes and Pigments*, vol. 170, p. 107591, 2019.
- [75] R. Kaur, A. Kaur, A. Umar, W. A. Anderson, and S. K. Kansal, "Metal organic framework (MOF) porous octahedral nanocrystals of Cu-BTC: Synthesis, properties and enhanced adsorption properties," *Materials Research Bulletin*, vol. 109, pp. 124-133, 2019.
- [76] Z. Li, X. Meng, and Z. Zhang, "Equilibrium and kinetic modelling of adsorption of Rhodamine B on MoS<sub>2</sub>," *Materials Research Bulletin*, vol. 111, pp. 238-244, 2019.
- [77] S. Yoon, J. J. Calvo, and M. C. So, "Removal of acid orange 7 from aqueous solution by metal-organic frameworks," *Crystals*, vol. 9, no. 1, p. 17, 2018.
- [78] H. Yang, H. Yuan, Q. Hu, W. Liu, and D. Zhang, "Synthesis of mesoporous C/MoS<sub>2</sub> for adsorption of methyl orange and photo-catalytic sterilization," *Applied Surface Science*, vol. 504, p. 144445, 2020.
- [79] T. H. Nawz *et al.*, "In Situ Synthesis of Crystalline MoS<sub>2</sub>@ ZIF-67 Nanocomposite for the Efficient Removal of Methyl Orange Dye from Aqueous Media," *Micromachines*, vol. 14, no. 8, p. 1534, 2023.
- [80] C. Santhosh, V. Velmurugan, G. Jacob, S. K. Jeong, A. N. Grace, and A. Bhatnagar, "Role of nanomaterials in water treatment applications: a review," *Chemical Engineering Journal*, vol. 306, pp. 1116-1137, 2016.
- [81] E. Forgacs, T. Cserháti, and G. Oros, "Removal of synthetic dyes from wastewaters: a review," *Environment international*, vol. 30, no. 7, pp. 953-971, 2004.
- [82] K. B. Tan, M. Vakili, B. A. Horri, P. E. Poh, A. Z. Abdullah, and B. Salamatina, "Adsorption of dyes by nanomaterials: recent developments and adsorption mechanisms," *Separation and purification technology*, vol. 150, pp. 229-242, 2015.
- [83] E. H. Ezechi, S. R. b. M. Kutty, M. H. Isa, and M. S. Liew, "Application of response surface methodology for the optimization of hexavalent chromium removal using a new low-cost adsorbent," *Desalination and Water Treatment*, vol. 57, no. 47, pp. 22507-22518, 2016.

- [84] A. Almasian, M. E. Olya, and N. M. Mahmoodi, "Synthesis of polyacrylonitrile/polyamidoamine composite nanofibers using electrospinning technique and their dye removal capacity," *Journal of the Taiwan Institute of Chemical Engineers*, vol. 49, pp. 119-128, 2015.
- [85] I. Ali, T. A. Khan, and M. Asim, "Removal of arsenic from water by electrocoagulation and electrodialysis techniques," *Separation & purification reviews*, vol. 40, no. 1, pp. 25-42, 2011.
- [86] V. Gupta and A. Nayak, "Cadmium removal and recovery from aqueous solutions by novel adsorbents prepared from orange peel and Fe<sub>2</sub>O<sub>3</sub> nanoparticles," *Chemical engineering journal*, vol. 180, pp. 81-90, 2012.
- [87] D. J. Yang, Z. F. Zheng, H. Y. Zhu, H. W. Liu, and X. P. Gao, "Titanate nanofibers as intelligent absorbents for the removal of radioactive ions from water," *Advanced Materials*, vol. 20, no. 14, pp. 2777-2781, 2008.
- [88] K. Y. Foo and B. H. Hameed, "Insights into the modeling of adsorption isotherm systems," *Chemical engineering journal*, vol. 156, no. 1, pp. 2-10, 2010.
- [89] X. Chen, "Modeling of experimental adsorption isotherm data," *information*, vol. 6, no. 1, pp. 14-22, 2015.
- [90] S. Patil, S. Renukdas, and N. Patel, "Removal of methylene blue, a basic dye from aqueous solutions by adsorption using teak tree (*Tectona grandis*) bark powder," *International journal of environmental sciences*, vol. 1, no. 5, pp. 711-726, 2011.
- [91] M. Rahimi, D. Wadi, and M. Vadi, "Langmuir, freundlich and temkin adsorption isotherm of captopril an ace inhibitor (or angiotensin-converting-enzyme inhibitor) is a pharmaceutical drug used for the treatment of hypertension by multi-wall carbon nanotube," *Indian Journal of Fundamental and Applied Life Sciences*, vol. 4, pp. 933-937, 2014.
- [92] S. E. Shaibu, F. A. Adekola, H. I. Adegoke, and O. S. Ayanda, "A comparative study of the adsorption of methylene blue onto synthesized nanoscale zero-valent iron-bamboo and manganese-bamboo composites," *Materials*, vol. 7, no. 6, pp. 4493-4507, 2014.
- [93] S. Umoren, U. Etim, and A. Israel, "Adsorption of methylene blue from industrial effluent using poly (vinyl alcohol)," *J. Mater. Environ. Sci*, vol. 4, no. 1, pp. 75-86, 2013.
- [94] A. Dada, A. Olalekan, A. Olatunya, and O. Dada, "Langmuir, Freundlich, Temkin and Dubinin–Radushkevich isotherms studies of equilibrium sorption of Zn<sup>2+</sup> unto phosphoric acid modified rice husk," *IOSR Journal of applied chemistry*, vol. 3, no. 1, pp. 38-45, 2012.

- [95] H. Kamal, "Removal of Methylene Blue from aqueous solutions using composite hydrogel prepared by gamma irradiation," *J Am Sci*, vol. 10, no. 4, pp. 125-133, 2014.
- [96] S. M. Kanawade and R. Gaikwad, "Removal of methylene blue from effluent by using activated carbon and water hyacinth as adsorbent," *International Journal of Chemical Engineering and Applications*, vol. 2, no. 5, p. 317, 2011.
- [97] A. Nisar, M. A. Khan, and Z. Hussain, "Synthesis and characterization of PANI/MOF-199/Ag nanocomposite and its potential application as non-enzymatic electrochemical sensing of dopamine," *Journal of the Korean Ceramic Society*, vol. 59, no. 3, pp. 359-369, 2022.
- [98] S. Kaushik, U. K. Tiwari, R. K. Choubey, K. Singh, and R. K. Sinha, "Study of sonication assisted synthesis of molybdenum disulfide (MoS<sub>2</sub>) nanosheets," *Materials Today: Proceedings*, vol. 21, pp. 1969-1975, 2020.
- [99] M. Abd Mutalib, M. A. Rahman, M. H. D. Othman, A. F. Ismail, and J. Jaafar, "Scanning Electron Microscopy (SEM) and Energy-Dispersive X-Ray (EDX) Spectroscopy," pp. 161-179, 2017.
- [100] J. Liu and J. M. Cowley, "High-resolution scanning transmission electron microscopy," *Ultramicroscopy*, vol. 52, no. 3-4, pp. 335-346 @ 0304-3991, 1993.
- [101] L. Laperrire and G. Reinhart, *CIRP encyclopedia of production engineering*. Springer Publishing Company, Incorporated, 2014.
- [102] J. P. Painuly, "Barriers to renewable energy penetration; a framework for analysis," *Renewable energy*, vol. 24, no. 1, pp. 73-89 @ 0960-1481, 2001.
- [103] F. J. Giessibl, "Advances in atomic force microscopy," *Reviews of modern physics*, vol. 75, no. 3, p. 949, 2003.
- [104] "<MIDEM\_30(2000)4p223.pdf>."
- [105] "<uv-vis\_student resource pack\_english.pdf>."
- [106] Q. M. Wang *et al.*, "Metallo-organic molecular sieve for gas separation and purification," *Microporous and mesoporous materials*, vol. 55, no. 2, pp. 217-230, 2002.
- [107] M. Han, S. Zhigang, and B. Shuang, "Understanding the exfoliation and dispersion of MoS<sub>2</sub> nanosheets in pure water," *Journal of Colloid and Interface Science*, vol. 517, pp. 204-212, 2018.

- [108] B. Difallah, M. Kharrat, M. Dammak, and G. Monteil, "Microstructure, friction and wear analysis of thermoplastic based composites with solid lubricant," *Mechanics & Industry*, vol. 13, p. 337, 2012.
- [109] S. Lin *et al.*, "Adsorption behavior of metal–organic frameworks for methylene blue from aqueous solution," *Microporous and mesoporous materials*, vol. 193, pp. 27-34, 2014.
- [110] S. Sarma, B. Ghosh, S. C. Ray, H. Wang, T. Mahule, and W. Pong, "Electronic structure and magnetic behaviors of exfoliated MoS<sub>2</sub> nanosheets," *Journal of Physics: Condensed Matter*, vol. 31, no. 13, p. 135501, 2019.
- [111] S. Homayoonnia and S. Zeinali, "Design and fabrication of capacitive nanosensor based on MOF nanoparticles as sensing layer for VOCs detection," *Sensors and Actuators B: Chemical*, vol. 237, pp. 776-786, 2016.
- [112] K. Lalithambika, K. Shanmugapriya, and S. Subramanian, "Photocatalytic activity of MoS<sub>2</sub> nanoparticles: an experimental and DFT analysis," *Applied Physics A*, vol. 125, 2019.